Cloud Retrieval Algorithms for MODIS: Optical Thickness, Effective Particle Radius, and Thermodynamic Phase

MICHAEL D. KING[1] AND SI-CHEE TSAY[2]
NASA Goddard Space Flight Center
Greenbelt, Maryland 20771

STEVEN E. PLATNICK[2] AND MENGHUA WANG[3]
University of Maryland Baltimore County
NASA Goddard Space Flight Center
Greenbelt, Maryland 20771

KUO-NAN LIOU
Department of Atmospheric Sciences
University of California Los Angeles
Los Angeles, California 90095-1565

MODIS Algorithm Theoretical Basis Document No. ATBD-MOD-05
MOD06 – Cloud product

(23 December 1997, version 5)

---

[1] Earth Sciences Directorate
[2] Laboratory for Atmospheres
[3] Laboratory for Hydrospheric Processes

TABLE OF CONTENTS

1. Introduction

The intent of this document is to present algorithms for inferring certain optical and thermodynamical properties of cloud layers, specifically, optical thickness, effective particle radius, and particle phase from multiwavelength reflected solar and emitted thermal radiation measurements.

It is well known that clouds strongly modulate the energy balance of the Earth and its atmosphere through their interaction with solar and terrestrial radiation, as demonstrated both from satellite observations (Ramanathan 1987, Ramanathan et al. 1989) and from modeling studies (Ramanathan et al. 1983, Cess et al. 1989). However, clouds vary considerably in their horizontal and vertical extent (Stowe et al. 1989, Rossow et al. 1989), in part due to the circulation pattern of the atmosphere with its requisite updrafts and downdrafts, and in part due to the distribution of oceans and continents and their numerous and varied sources of cloud condensation nuclei (CCN). A knowledge of cloud properties and their variation in space and time, therefore, is crucial to studies of global climate change (e.g., trace gas greenhouse effects), as general circulation model (GCM) simulations indicate climate-induced changes in cloud amount and vertical structure (Wetherald and Manabe 1988), with a corresponding cloud feedback working to enhance global warming.

GCM simulations by Roeckner et al. (1987) and Mitchell et al. (1989) include corresponding changes in cloud water content and optical thickness, and suggest that changes in cloud optical properties may result in a negative feedback comparable in size to the positive feedback associated with changes in cloud cover. None of the GCM simulations to date include corresponding changes in cloud microphysical properties (e.g., particle size), which could easily modify conclusions thus far obtained. Of paramount importance to a comprehensive understanding of the Earth's climate and its response to anthropogenic and natural variability is a knowledge, on a global sense, of cloud properties that may be achieved through remote sensing and retrieval algorithms.

In this document we start with a background overview of the MODIS instrumentation and the cloud retrieval algorithms, followed by a description of the theoretical basis of the cloud retrieval algorithms to be applied to MODIS data. We follow with a discussion of practical considerations (including the constraints and limitations involved in the retrieval algorithms), outline our validation strategy, and present our plans for refinement of the algorithms during the pre-launch and post-launch development phases.

2. Overview and background information

The purpose of this document is to provide a description and discussion of the physical principles and practical considerations behind the remote sensing and retrieval algorithms for cloud properties that we are developing for MODIS. Since the development of the algorithms, to be used in analyzing data from the MODIS sensor system, is at the at-launch software development stage, this document is based on methods that have previously been developed for processing data from other sensors with similar spectral characteristics. Through continued interaction with the MODIS science team and external scientific community, we anticipate that these algorithms will be further refined for use in the processing of MODIS data, both through simulations and through airborne field experiments.

2.1. Experimental objectives

The main objective of this work is the development of routine and operational methods for simultaneously retrieving the cloud optical thickness and effective particle radius from daytime multiwavelength reflected solar and emitted thermal radiation measurements. Retrieval of cloud particle phase from visible and near-infrared solar reflection measurements will also be discussed. Methods presented here are based in part on the work of Nakajima and King (1990) and the review article of King et al. (1992), as well as on recent work utilizing the 3.7 µm band of the Advanced Very High Resolution Radiometer (AVHRR) for the remote sensing of cloud optical and microphysical properties, described by Platnick and Twomey (1994) and Nakajima and Nakajima (1995).

Figure 1 illustrates the data flow diagram for all of the MODIS atmosphere algorithms, including production of the cloud mask product (MOD35) and the MODIS cloud product (MOD06). Knowledge of particle phase, along with cloud cover, are necessary inputs for retrieving the cloud optical thickness and effective particle radius. Cloud cover will be provided by the cloud top properties algorithm of Menzel and Strabala (1997) based on analysis of the cloud mask algorithm of Ackerman et al. (1997). An algorithm for cloud particle phase, using emitted thermal radiation measurements, is also being developed by Menzel and Strabala (1997); our algorithm for thermodynamic phase complements theirs by adding reflected solar radiation measurements, and the two will eventually be included as separate parameters in the cloud product (MOD06).

The importance of retrieving the optical thickness and effective radius derives not only from the fact that such a retrieval is possible, but from the fact that shortwave cloud radiative properties depend almost exclusively on these two parameters. This thus forms the basis of cloud radiative parameterization methods, such as the one developed by Slingo (1989), which require that a global data base on the effective radius and optical thickness (or equivalently integrated liquid water content) of clouds be available. Such data seem only to be derivable from spaceborne remote sensing observations. Therefore, MODIS is ideally suited to cloud remote sensing applications and retrieval purposes.

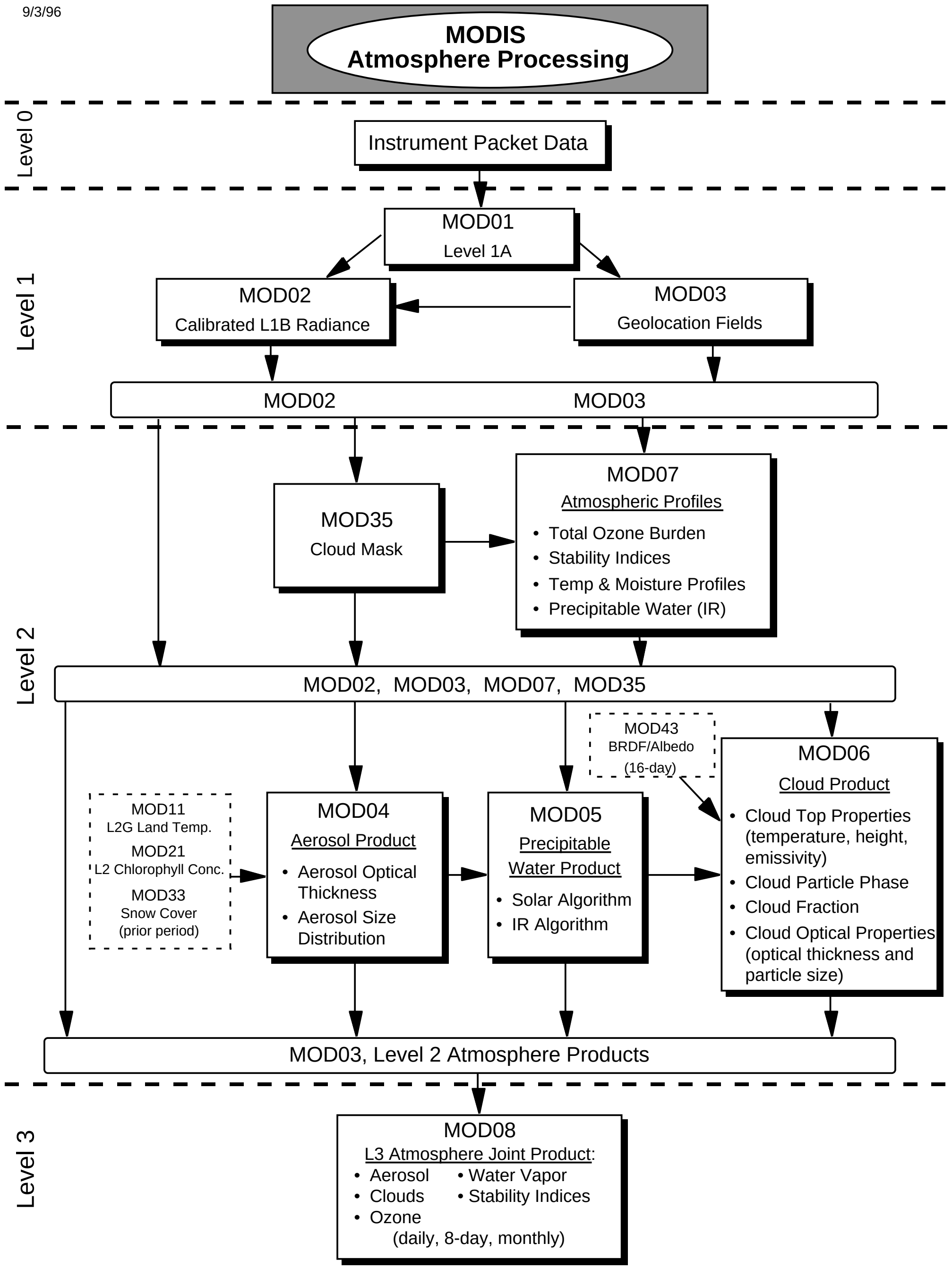
9/3/96

Figure 1. Data flow diagram for the MODIS atmosphere products, including product MOD06, some parameters of which (optical thickness and effective particle size) are produced by the algorithm described in this ATBD-MOD-06.

2.2. Historical perspective

Ever since the first launch of the TIROS-1 satellite in 1960, tremendous interest has arisen in the field of using these remotely sensed data to establish a global cloud climatology, in which a qualitative cloud atlas was archived. It has been a long-standing goal to quantify global cloud properties from spaceborne observations, such as cloud cover, cloud particle thermodynamic phase, cloud optical thickness and effective particle radius, and cloud top altitude and temperature. Many efforts in the past three decades (e.g., work dated as early as 1964 by Arking) have been devoted to extracting cloud cover parameters from satellite measurements.

There are a number of studies of the determination of cloud optical thickness and/or effective particle radius with visible and near-infrared radiometers on aircraft (Hansen and Pollack 1970, Twomey and Cocks 1982 and 1989, King 1987, Foot 1988, Rawlins and Foot 1990, Nakajima and King 1990, Nakajima et al. 1991) and on satellites (Curran and Wu 1982, Rossow et al. 1989). Further, the utility of the 3.7 µm band onboard the AVHRR has been demonstrated by several investigators, including Arking and Childs (1985), Durkee (1989), Platnick and Twomey (1994), Han et al. (1994, 1995), Nakajima and Nakajima (1995) and Platnick and Valero (1995). The underlying principle on which these techniques are based is the fact that the reflection function of clouds at a nonabsorbing band in the visible wavelength region is primarily a function of the cloud optical thickness, whereas the reflection function at a water (or ice) absorbing band in the near-infrared is primarily a function of cloud particle size.

Twomey and Cocks (1989) developed a statistical method for simultaneously determining the cloud optical thickness and effective radius using reflected intensity measurements at several wavelengths in the near-infrared region. An extension of this technique addresses the problem of identifying the thermodynamic phase of clouds (ice *vs* water) and of distinguishing clouds from snow surfaces by utilizing particular bands (e.g., 1.64 and 2.2 µm) which provide different absorption characteristics of water and ice (e.g., Pilewskie and Twomey 1987).

Although these studies have demonstrated the applicability of remote sensing methods to the determination of cloud optical and microphysical properties, more theoretical and experimental studies are required in order to assess the soundness and accuracy of these methods when applied to measurements on a global scale. From the theoretical point of view, the application of asymptotic theory to the determination of cloud optical thickness (King 1987) has demonstrated the physical basis of the optical thickness retrieval and its efficient implementation to experimental observations. This method is worth incorporating as one component of any multiwavelength algorithm for simultaneously determining the cloud particle phase, optical thickness and effective particle radius. From the experimental point of view, more aircraft validation experiments are required in order to assess the validity of these methods, since many factors affect the successful retrieval of these parameters when applied to real data in a real atmosphere (e.g., Rossow et al. 1985, Wu 1985).

Since 1986, an extensive series of field observations has been conducted. These include: FIRE-I/II Cirrus (First ISCCP Regional Experiment, 1986 and 1991, respectively), FIRE-I Stratocumulus (1987), ASTEX (Atlantic Stratocumulus Transition Experiment, 1992), TOGA/COARE (Tropical Ocean Global Atmosphere/Coupled Ocean-Atmosphere Response Experiment, 1993), CEPEX (Central-Equatorial Pacific Experiment, 1993), SCAR-A (Sulfate, Clouds And Radiation-Atlantic, 1993), MAST (Monterey Area Ship Track Experiment, 1994), SCAR-C (Smoke, Clouds And Radiation - California, 1994), ARMCAS (Arctic Radiation

Measurements in Column Atmosphere-surface System, 1995), SCAR-B (Smoke, Clouds And Radiation - Brazil, 1995), and SUCCESS (Subsonic Aircraft Contrail and Cloud Effects Special Study, 1996). Instrumentation involved in these experiments has included either the MCR (Multispectral Cloud Radiometer; Curran et al. 1981) or MAS (MODIS Airborne Simulator; King et al. 1996), airborne sensors having spectral characteristics similar to a number of the cloud retrieval bands contained in MODIS, as well as the NOAA AVHRR satellite sensor. In the pre-launch stage of MODIS, these observational data, especially MAS data for which more than 500 research hours have thus far been obtained under various all-sky conditions, form the basis for our cloud retrieval algorithm development and validation.

2.3. Instrument characteristics

MODIS is a 36-band scanning spectroradiometer. Four of these visible (0.645 µm) and near-infrared (1.64, 2.13, and 3.75 µm) spectral bands will be used in our daytime shortwave cloud retrieval algorithm over land surfaces, with 0.858 or 1.240 µm replacing 0.645 µm over ocean and bright snow/sea ice surfaces, respectively. Other bands in the thermal region, such as the 8.55, 11.03, 12.02, 13.335, 13.635, 13.935 and 14.235 µm bands, will be used for cloud cover and cloud top properties (including cloud top altitude, cloud top temperature and thermodynamic phase), as discussed elsewhere (Ackerman et al. 1997; Menzel and Strabala 1997). In addition, the 11.03 µm band will be used to make the thermal emission correction to the 3.75 µm band during the day (see Section 3.1.2.c).

Figure 2 shows the wavelength locations of these primary MODIS shortwave bands, located in the water vapor window regions. The band center and band-

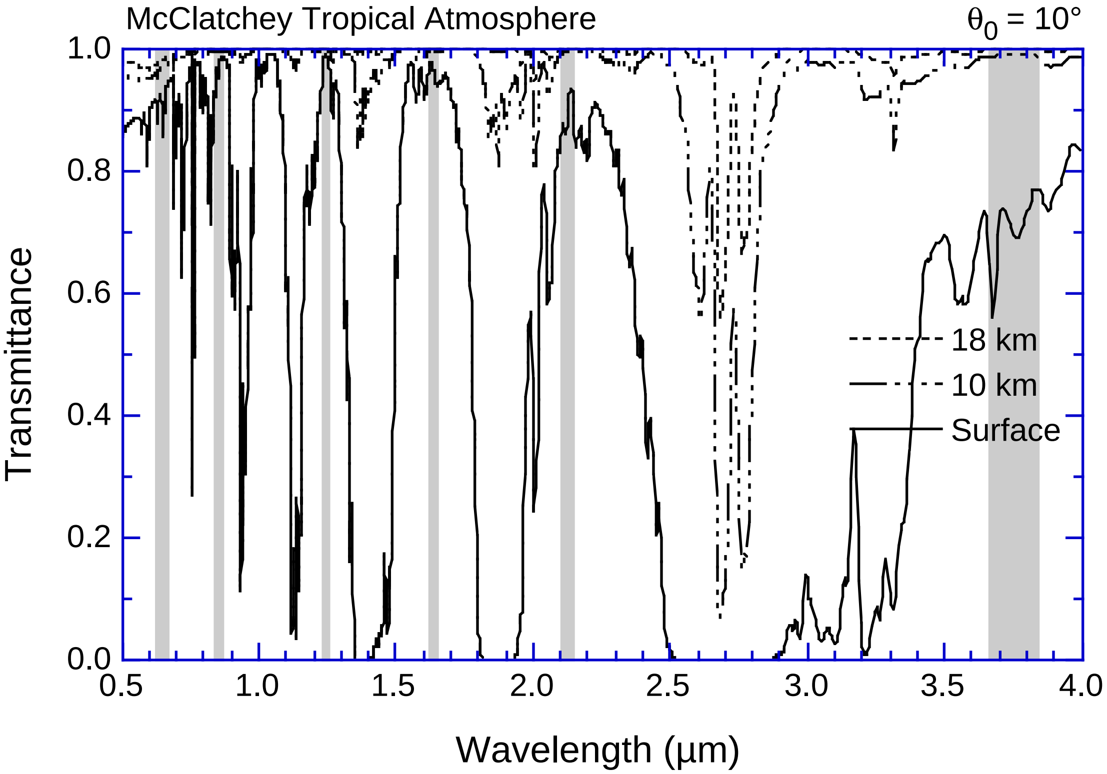

Figure 2. Spectral characteristics of six MODIS bands, centered at 0.65, 0.86, 1.24, 1.64, 2.13, and 3.75 µm, used for cloud property detection. The atmospheric transmittances are calculated from LOWTRAN 7 at 18 km, 10 km and at the surface for the McClatchey tropical atmosphere at 10° solar zenith angle.

width characteristics, as well as the dynamic range and main purpose(s) of each band, are also summarized in Table 1. The 0.645, 2.13 and 3.75 µm bands will be used to retrieve the cloud optical thickness and effective particle radius over land (with 0.645 µm replaced by 0.858 µm over oceans and 1.24 µm over snow and sea ice surfaces); a combination of the 0.645, 1.64, and possibly the 2.13 µm bands will be used for cloud thermodynamic phase determination.

MODIS is designed to scan through nadir in a plane perpendicular to the velocity vector of the spacecraft, with the maximum scan extending up to 55° on either side of nadir (110° aperture). At a nominal orbital altitude for the EOS AM-1 spacecraft of 705 km, this yields a swath width of 2330 km centered on the satellite ground track. In the baseline concept, the Earth-emitted and reflected solar radiation is incident on a two-sided scan mirror that continually rotates

Table 1. Spectral characteristics, spatial resolution, saturation reflection function (at θ_0 = 22.5°), saturation brightness temperature, and principal purposes of cloud bands used on MODIS.

Band	λ (µm)	$\Delta\lambda$ (µm)	Ground resolution (m)	$R_{\max}$	$T_{\max}$ (K)	Atmospheric Purpose
1	0.645	0.050	250	1.43		Cloud optical thickness over land
2	0.858	0.035	250	0.96		Cloud optical thickness over ocean
5	1.240	0.020	500	0.78		Cloud optical thickness over snow & sea ice surfaces
6	1.640	0.025	500	1.02		Snow / cloud discrimination; thermodynamic phase
7	2.130	0.050	500	0.81		Cloud effective radius
20	3.750	0.180	1000		335	Cloud effective radius; Cloud / surface temperature
31	11.030	0.500	1000		400	Thermal correction

about an axis aligned with the direction of flight. Following the scan mirror is a telescope and a sequence of three dichroic beam splitters that further subdivide the incoming radiation into four focal planes. The 3.75 µm band uses a ten-element linear array detector for the 1000 m spatial resolution bands, a 20-element array for the 500 m bands at the 1.64 and 2.13 µm bands, and a 40-element array for the 250 m band at 0.645 µm. They are aligned parallel to one another such that a single scan of the scan mirror is imaged on the focal plane for a swath 10 km in the along-track direction and 2330 km in the cross-track direction. In this configuration, all bands within a single focal plane are simultaneously sampled and registered within 0.1 pixel, with registration errors of less than 0.2 pixels between focal planes. The signal-to-noise ratio ranges between 57 and 1100 at a solar zenith angle θ_0 = 70°, depending on band, and is considerably larger than these values at the solar zenith angle and scene temperature typical of the EOS AM-1 orbit (θ_0 = 22.5°).

Prior to executing the algorithms discussed below, the MODIS data processing system, as part of the level-1b calibrated radiance process (MOD_PR02), integrates the 250 and 500 m bands to produce an equivalent 1000 m band using the point spread function of MODIS. The output product MOD06 is hence stored in 3 separate files at 250 m (2 bands), 500 m (7 bands), and 1000 m (36 bands), together with geolocation information every 5 km along track and every 5th pixel cross track. In this way, all algorithms that use multispectral combinations of bands will be operating at a uniform spatial resolution. The native higher resolution bands will be used only for process studies associated with validation campaigns comprising coincident cloud microphysical measurements (see Section 3.3.2).

3. Algorithm description

In this section we will concentrate mainly on discussing the algorithm for simultaneously retrieving daytime cloud optical thickness and effective particle radius from multiwavelength reflected solar radiation measurements. In addition to the usual table lookup approach, we will utilize interpolation and asymptotic theory to fulfill this task, where appropriate. This procedure is especially direct and efficient for optically thick layers, where asymptotic expressions for the reflection function are the most valid, but can be applied to the full range of optical thicknesses using interpolation of radiative transfer calculations.

3.1. Theoretical description

3.1.1. Physics of problem

a. Cloud optical thickness and effective particle radius

Strictly speaking, our algorithm is mainly intended for plane-parallel liquid water clouds. It is assumed that all MODIS data analyzed by our algorithm has been screened by the cloud mask of Ackerman et al. (1997) with additional information regarding particle phase from the algorithm of Menzel and Strabala

(1997), one component of developing product MOD06, as outlined in Figure 1.

To retrieve the cloud optical thickness and effective particle radius, a radiative transfer model is first used to compute the reflected intensity field. It is convenient to normalize the reflected intensity (radiance) $I^{\lambda}(0, -\mu, \phi)$ in terms of the incident solar flux $F_0(\lambda)$, such that the reflection function $R^{\lambda}(\tau_c, r_e; \mu, \mu_0, \phi)$ is defined by

$$R^{\lambda}(\tau_c, r_e; \mu, \mu_0, \phi) = \frac{\pi I^{\lambda}(0, -\mu, \phi)}{\mu_0 F_0(\lambda)} , \tag{1}$$

where τ_c is the total optical thickness of the atmosphere (or cloud), r_e the effective particle radius, defined by (Hansen and Travis 1974)

$$r_e = \int_0^{\infty} r^3 n(r)\,\mathrm{d}r \Big/ \int_0^{\infty} r^2 n(r)\,\mathrm{d}r , \tag{2}$$

where $n(r)$ is the particle size distribution and r is the particle radius, μ_0 the cosine of the solar zenith angle θ_0, μ the absolute value of the cosine of the zenith angle θ, measured with respect to the positive τ direction, and ϕ the relative azimuth angle between the direction of propagation of the emerging radiation and the incident solar direction.

When the optical thickness of the atmosphere is sufficiently large, numerical results for the reflection function must agree with known asymptotic expressions for very thick layers (van de Hulst 1980). Numerical simulations as well as asymptotic theory show that the reflection properties of optically thick layers depend essentially on two parameters, the scaled optical thickness τ_c' and the similarity parameter s, defined by

$$\tau_c' = (1 - \omega_0 g)\tau_c , \tag{3}$$

$$s = \left(\frac{1 - \omega_0}{1 - \omega_0 g}\right)^{1/2} , \tag{4}$$

where g is the asymmetry factor and ω_0 the single scattering albedo of a small volume of cloud air. In addition, the reflectance properties of the Earth-atmosphere system depend on the reflectance (albedo) of the underlying surface, A_g. The similarity parameter, in turn, depends primarily on the effective particle radius. In addition to τ_c', s and A_g, the details of the single scattering phase function affect the directional reflectance of the cloud layer (King 1987).

Our assumption here is that the reflection function is not dependent on the exact nature of the cloud particle size distribution, depending primarily on the effective radius and to a lesser extent on the effective variance, as first suggested by Hansen and Travis (1974). Nakajima and King (1990) showed that the similarity parameter is virtually unaffected by the effective variance (or standard deviation) of the cloud particle size distribution, but the asymmetry parameter, and hence scaled optical thickness, is weakly affected by the detailed shape of the size distribution.

For a band with a finite bandwidth, Eq. (1) must be integrated over wavelength and weighted by the band's spectral response $f(\lambda)$ as well as by the incoming solar flux $F_0(\lambda)$. Hence, we can rewrite Eq. (1) as

$$R(\tau_c, r_e; \mu, \mu_0, \phi) = \frac{\int_\lambda R^\lambda(\tau_c, r_e; \mu, \mu_0, \phi) f(\lambda) F_0(\lambda)\, d\lambda}{\int_\lambda f(\lambda) F_0(\lambda)\, d\lambda}. \tag{5}$$

Values of the reflection function must be stored at three geometrical angles (θ_0, θ, ϕ), M optical thicknesses (τ_c), N prescribed effective particle radii (r_e), and K surface albedos (A_g). This forms a rather large lookup table and potentially causes sorting and computational inefficiencies.

The determination of τ_c and r_e from spectral reflectance measurements constitutes the *inverse* problem and is typically solved by comparing the measured reflectances with entries in a lookup table and searching for the combination of τ_c and r_e that gives the best fit (e.g., Twomey and Cocks 1982, 1989). An alternative approach was suggested by Nakajima and King (1990), who showed that by applying asymptotic theory of optically thick layers, computations of the reflection function for a given value of τ_c, r_e and A_g can be determined efficiently and accurately, thereby reducing the size of the lookup tables required, and hence enabling application of analytic inversion and interpolation methods. This in no way alters the results of the retrieval, but simply makes use of efficient interpolation to reduce the size of the lookup tables and enhances the physical insight of the retrieval.

Figure 3 illustrates the spherical albedo as a function of wavelength for water clouds containing various values of the effective radius. Since the spherical albedo represents a mean value of the reflection function over all solar and observational zenith and azimuth angles, the reflection function itself must have a similar sensitivity to particle size. These computations were performed using asymptotic theory for thick layers and the complex refractive indices of liquid water, and include the additional contribution of water vapor. These computations strictly apply to the case when τ_c (0.75 µm) = 16 and A_g = 0.0, and properly allow for the optical thickness and asymmetry factor to vary with wavelength in accord with our expectations for clouds composed solely of liquid water and water vapor (cf. King et al. 1990 for details). Since the similarity parameter is nearly zero (conservative scattering) in the water vapor windows at wavelengths $\lambda \lesssim$ 1.0 µm, the cloud optical thickness can be derived primarily from reflection function measurements in this wavelength region. Figure 3 also shows that the spherical albedo, and hence reflection function, is sensitive to particle size at wavelengths near 1.64, 2.13, and 3.75 µm, wavelengths for which water vapor ab-

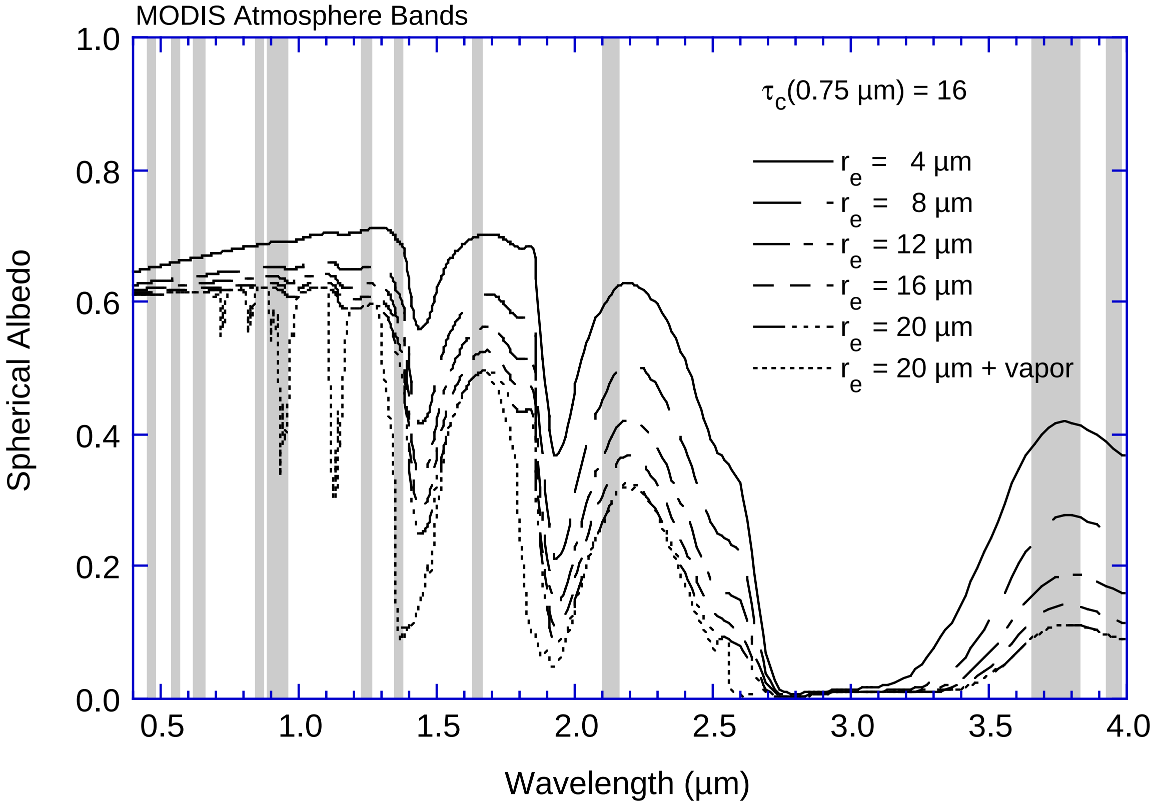

Figure 3. Cloud spherical albedo as a function of wavelength for selected values of the effective radius of cloud droplets. Results apply to water clouds having a modified gamma size distribution with an effective variance v_e = 0.111, cloud optical thickness τ_c(0.75 µm) = 16, and saturated water vapor w_g = 0.45 g cm^{-2}. The location and bandwidth of selected MODIS atmosphere bands are also shown in the figure.

sorption is small.

Cloud properties can also be estimated from the thermal bands. Figure 4 shows the top-of-the-atmosphere brightness temperature as a function of wavenumber (wavelength) from 600-3340 cm^{-1} (3-16.7 µm) for both clear and cloud sky conditions, where all computations were made using the discrete ordinates radiative transfer model developed by Tsay et al. (1990). These computations apply to mid-latitude summer conditions, an ocean-like surface having a temperature of 294 K, unit emissivity (zero reflectance), and overhead sun. These computations further include gaseous absorption (water vapor, carbon dioxide, ozone, and the infrared water vapor continuum) at a 20 cm^{-1} spectral resolution

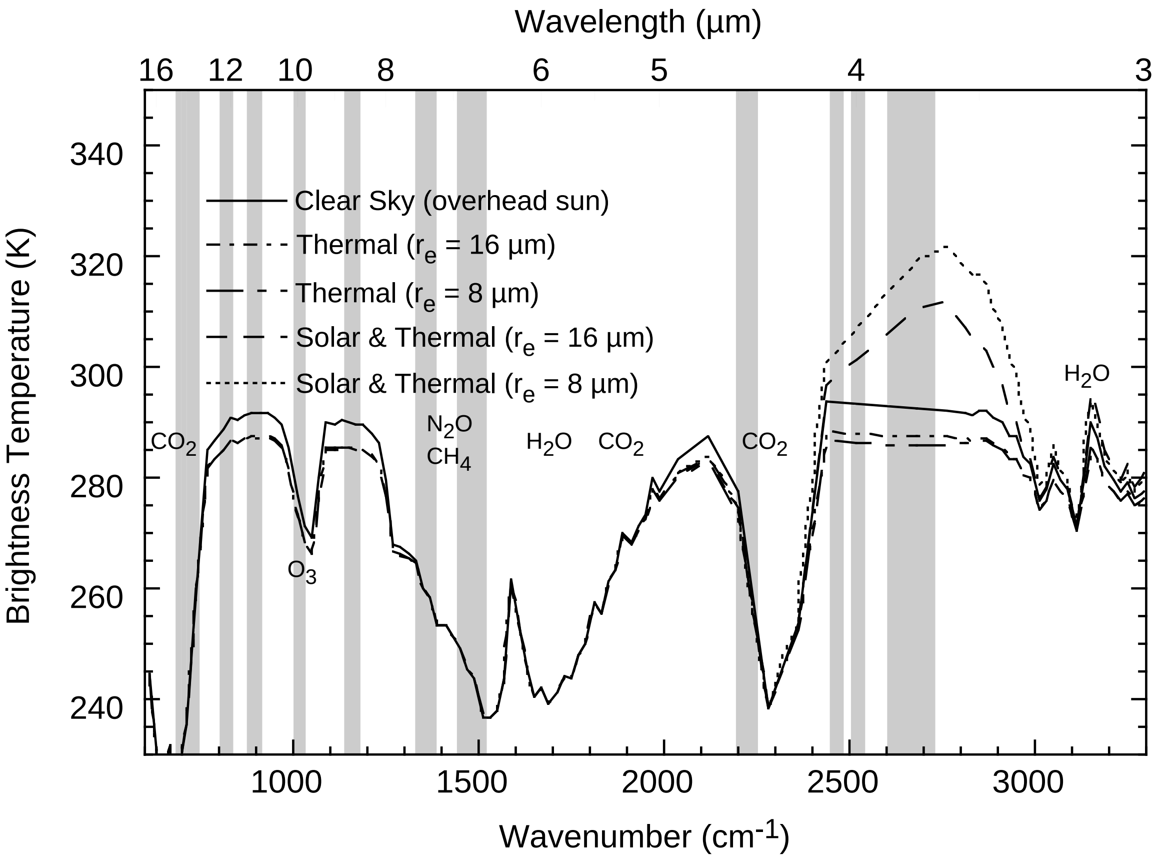

Figure 4. Brightness temperature as a function of wavelength for nadir observations and for various values of the effective radius of cloud droplets, where the cloud optical thickness τ_c(0.75 µm) = 5 for all cases. Results apply to water clouds having a modified gamma distribution embedded in a midlatitude summer atmosphere with cloud top temperature T_t = 14°C, cloud base temperature T_b = 17°C, and an underlying surface temperature T_s = 21°C (assumed black). The location and bandwidth of all MODIS thermal bands are also shown in the figure.

(Tsay et al. 1989), with a low-level water cloud of optical thickness 5 (at 0.75 µm) placed at an altitude between 1 and 1.5 km.

In the 3.7 µm window, both solar reflected and thermal emitted radiation are significant, though the use of the reflectance for cloud droplet size retrieval is seen to be much more sensitive than the thermal component (note that, in either case, the thermal and solar signals must be separated to provide the desired component). CO_2 absorption is important around 4.3 µm and at wavelengths greater than about 13 µm; the MODIS bands in these spectral regions can indicate

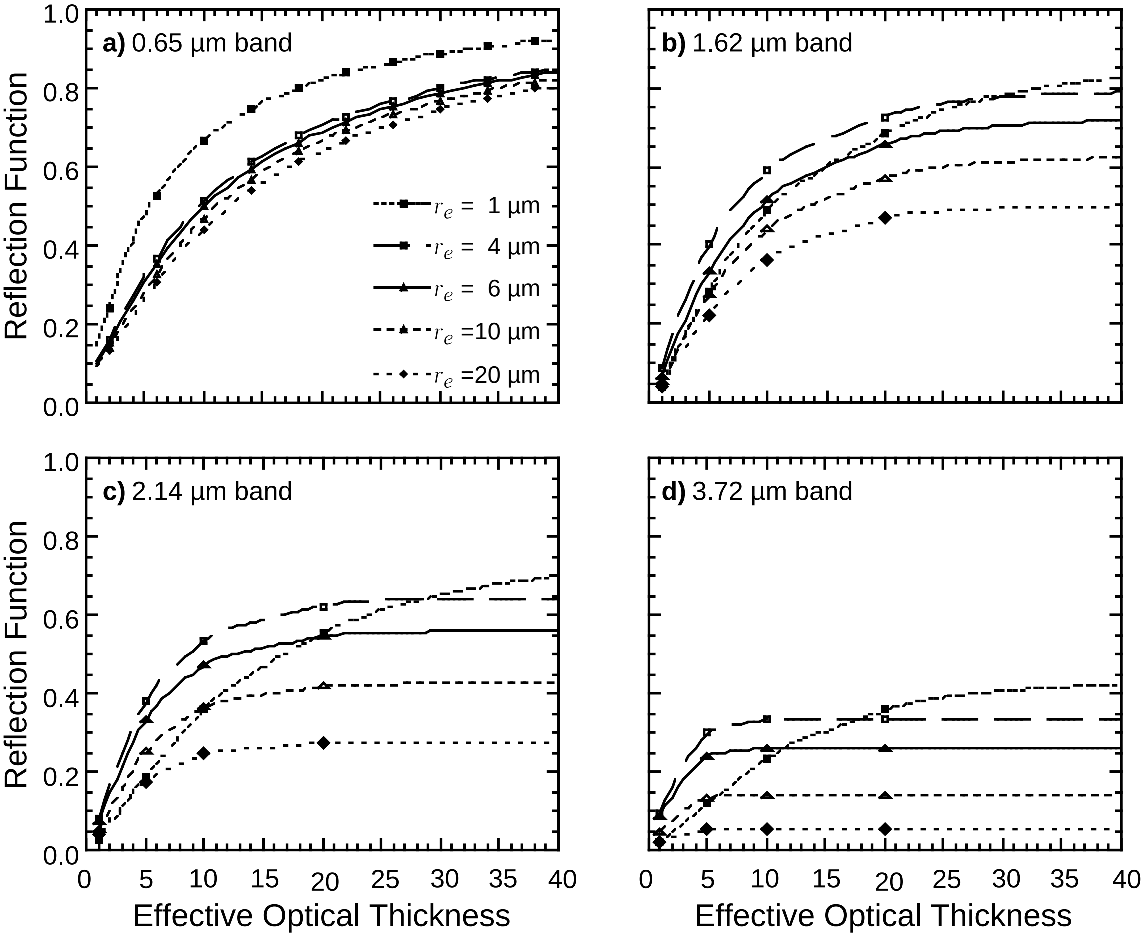

Figure 5. Reflection function as a function of effective optical thickness at a visible wavelength for (a) 0.65 µm, (b) 1.62 µm, (c) 2.14 µm, and (d) 3.72 µm.

vertical changes of temperature.

Figure 5 shows the reflection function as a function of optical thickness and effective radius for the MODIS Airborne Simulator bands used in cloud retrieval validation studies. Calculations were performed using the optical constants of liquid water compiled by Irvine and Pollack (1968), together with the assumption that the underlying surface reflectance $A_g = 0.0$. As previously noted, the optical thickness of a cloud depends on wavelength as well as the cloud particle size distribution $n(r)$, as reflected in the effective radius [see King et al. (1990) for an illustration of the spectral dependence of τ_c, g, s and τ_c']. In order to compare the curves of Fig. 5 for various wavelengths, the optical thickness $\tau_c(\lambda)$ is scaled by $2/Q_{\mathrm{ext}}(r_e/\lambda)$ to provide a common abscissa [roughly equivalent to $\tau_c(\lambda_{\mathrm{vis}})$], where $Q_{\mathrm{ext}}(r_e/\lambda)$ is the extinction efficiency factor. For the visible band, scattering is nearly conservative so that separation of the reflection function curves in Fig. 5a is due to an increasing asymmetry factor with droplet size (for $r_e \gtrsim 4$ µm). For the near-infrared bands, the similarity parameter (and hence droplet absorption) increases approximately linearly with effective radius, and hence the asymptotic reflectance of a cloud decreases with increasing particle size. These figures show that the visible band contains information primarily regarding cloud optical thickness, whereas the absorbing bands eventually reach an optical thickness where they are primarily dependent on particle size alone. A combination of visible and near-infrared absorbing bands therefore provides information on both optical thickness and effective radius.

A close examination of Figs. 5b-d also reveals that the reflection function for a single absorbing wavelength is, in general, not unique. In all near-infrared bands, an effective radius of 1 µm is seen to have the same reflection function, at some optical thickness, as some other radius. This has been observed by a number of investigators, all of whom eliminated the small droplet size on the basis of physical arguments that these small sizes do not typically occur in real terrestrial clouds (e.g., Twomey and Cocks 1989, using 1.2, 1.6 and 2.2 µm; Nakajima and King 1990, using 2.2 µm; Platnick and Twomey 1994, using 3.7 µm). Nakajima and King (1990) showed that a combination of 1.6, 2.2 and 3.7 µm bands in a single cloud retrieval should eliminate this ambiguity (multivalued solution) in the retrieved particle radius (see below).

b. Cloud thermodynamic phase

During the post-launch time period, we plan to perfect a robust and routine algorithm for determining cloud thermodynamic phase (water *vs* ice). The physical principle upon which this technique is based is the fact that the differences in reflected solar radiation between the 0.645 and 1.64 µm bands contain information regarding cloud particle phase due to distinct differences in bulk absorption characteristics between water and ice at the longer wavelength. The visible reflectance, suffering no appreciable absorption for either ice or liquid water, is relatively unaffected by thermodynamic phase. However, if the cloud is composed of ice, or if the surface is snow covered (similar in effect to large ice particles), then the reflectance of the cloud at 1.64 µm will be smaller than for an otherwise identical liquid water cloud. The 2.13 µm band is expected to show a significant decrease in reflectance as well, but this is somewhat less dramatic than the reduced reflectance at 1.64 µm. Demonstrations of the application of this method to the problem of distinguishing the thermodynamic phase of clouds can be found in Hansen and Pollack (1970), Curran and Wu (1982), and Pilewskie and Twomey (1987). For added phase discrimination, it is expected that a retrieval of cloud effective radius using the 1.64 µm band alone will yield a substantially different result than one obtained using only the 2.13 µm band.

As an example of the sensitivity of the 1.64 and 2.13 µm bands of MODIS to the thermodynamic phase of clouds, we have examined MAS data obtained over the northern foothills of the Brooks Range, Alaska, on 8 June 1995. These data were acquired as part of a NASA ER-2 airborne campaign to study arctic stratus clouds over sea ice in the Beaufort Sea. The panel in the upper left portion of Fig. 6, acquired at 0.66 µm, shows high contrast between an optically thick convective cumulonimbus cloud in the center of the image, a diffuse cirrus anvil in the lower part of the image, less reflective altocumulus clouds in the upper part of the image, and dark tundra. From data obtained down the nadir track of the air-

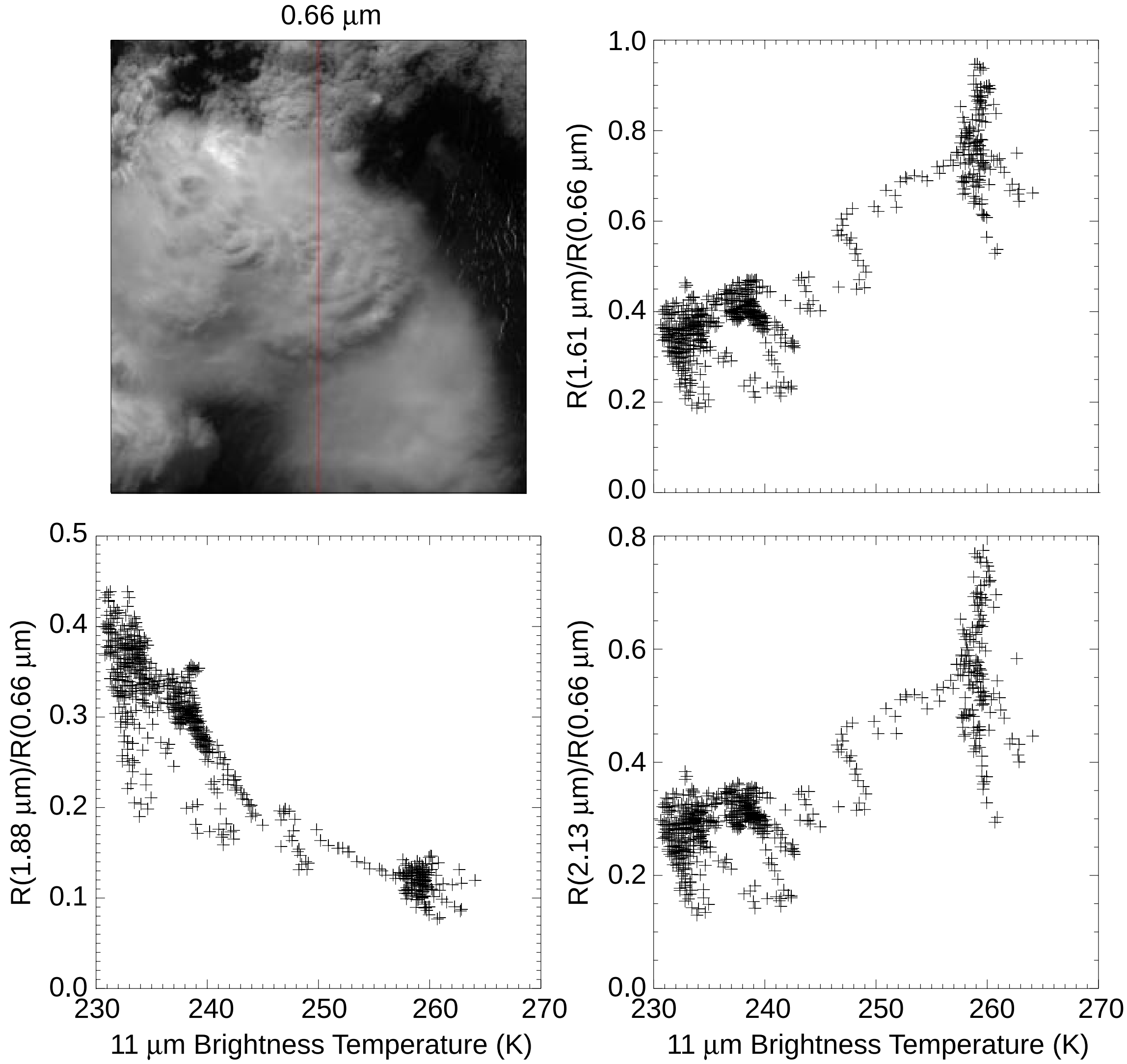

Figure 6. The upper left-hand panel shows a MAS 0.66 µm image of a convective cumulonimbus cloud surrounded by lower-level water clouds on the north slope of the Brooks Range on 7 June 1995. Subsequent panels show scatter plots of the reflection function ratio $R^{1.61}/R^{0.66}$, $R^{1.88}/R^{0.66}$, and $R^{2.13}/R^{0.66}$ as a function of the corresponding brightness temperature at 11.02 µm for nadir observations of the MAS over a cloud scene containing both water and ice clouds.

craft (vertical line down the center of the image), we have produced scatter plots of the ratio of the reflection function at 1.61, 1.88, and 2.13 µm to that at 0.66 µm as a function of the brightness temperature at 11.02 µm. These observations clearly shows that the cold portion of the scene contained ice particles (low reflectance at 1.61 and 2.13 µm), whereas the warm portion contained water droplets (high reflectance at 1.61 and 2.13 µm), as expected. In addition, the 1.88 µm band, the closest analog to the 1.38 µm water vapor absorbing band on MODIS, suggests that the colder ice clouds were high in the atmosphere (high 1.88 µm reflectance), whereas the warmer water clouds were low in the atmosphere (low 1.88 µm reflectance).

c. *Ice cloud properties*

After the cloud mask and phase determination, the physical and optical properties of ice clouds can, in principle, be retrieved in a manner similar to that described previously for water clouds. Under the assumption of plane-parallel geometry, two other factors complicate the retrievals of ice cloud properties (viz., the shape and orientation of the ice particles) occurring naturally in the atmosphere. Due to our limited knowledge accumulated thus far for ice clouds, the sensitivity of their retrieved properties on these two factors is still an ongoing research subject.

Following the same manner as in water clouds, we have selected a size distribution of the ice particles for the purpose of discussion. Figure 7 shows an observed size distribution for averaged cirrus clouds obtained during the FIRE-II Cirrus IFO on 5 December 1991. This model cloud is composed of 50% bullet rosettes, 30% hollow columns, and 20% solid plate ice crystals. We then define the effective particle diameter as follows

$$D_e = \int_0^\infty LD^2 n(L)dL \Big/ \int_0^\infty LDn(L)dL, \qquad (6)$$

where D and L denote the width and the maximum dimension of an ice crystal, respectively, and $n(L)$ is the size distribution as a function of L. The rationale for defining D_e to represent ice-crystal size distribution is that the scattering of light is related to the geometric cross section, which is proportional to LD. To calcu-

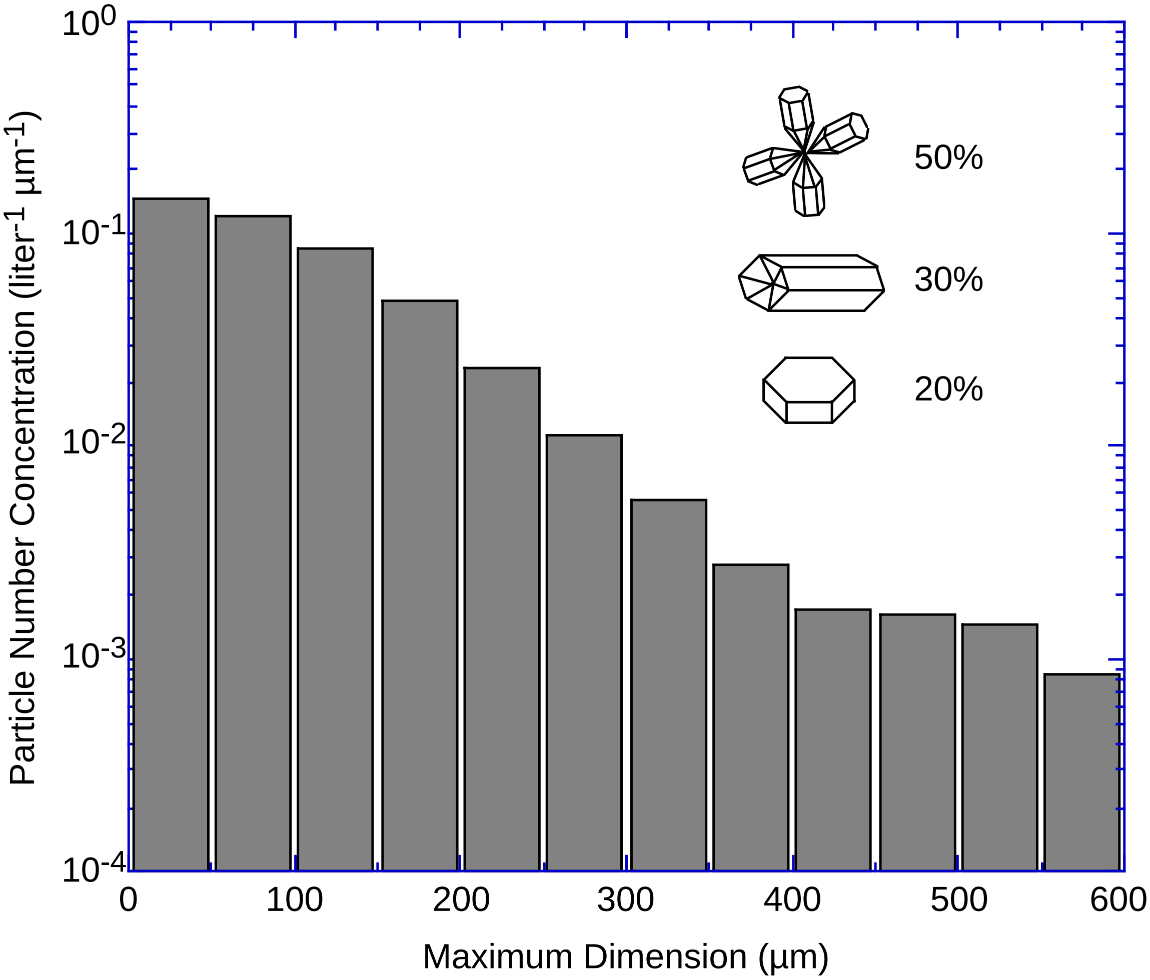

Figure 7. An averaged ice-crystal size distribution observed during the FIRE-II Cirrus IFO (5 December 1991), as determined from the replicator sounding.

late properties of light scattering and absorption by ice crystals, we have adopted a unified theory developed by Takano and Liou (1989, 1995), and Yang and Liou (1995, 1996a,b) for all sizes and shapes. This unified theory is a unification of an improved geometric ray-tracing / Monte Carlo method for size parameters larger than about 15 and a finite-difference time domain method for size parameters less than 15.

In Table 2, we demonstrate the bulk optical properties of this ice cloud model, calculated for six selected MODIS bands. Their corresponding phase functions are illustrated in Fig. 8. Thus, the reflected reflectance fields [e.g., Eq.

Table 2. Optical properties of a representative ice crystal size distribution for six MODIS bands.

Band	λ (µm)	m_r	m_i	β_e	ω_0	g
1	0.645	1.3082	1.325×10^{-8}	0.32827	0.99999	0.84580
5	1.240	1.2972	1.22×10^{-5}	0.33141	0.99574	0.85224
6	1.640	1.2881	2.67×10^{-4}	0.32462	0.93823	0.87424
7	2.130	1.2674	5.65×10^{-4}	0.32934	0.91056	0.89044
20	3.750	1.3913	6.745×10^{-3}	0.32971	0.68713	0.90030
31	11.030	1.1963	2.567×10^{-1}	0.32812	0.54167	0.95739

(5)] for ice clouds can be pre-computed for later use in retrieval algorithms similar to those of water clouds. It is worth noting that Ou et al. (1993) recently developed a retrieval technique that utilizes the thermal infrared emission of ice clouds to determine their optical thickness and effective particle size. Removal of the solar component in the 3.75 µm intensity is required for daytime applications, which is made by correlating the 3.75 µm (solar) and 0.645 µm reflectances. However, it is clear that the use of the reflectance for particle size retrieval is seen from Fig. 4 to be much more sensitive than the thermal infrared component. Careful intercomparison of cloud retrievals between these two methods is currently underway.

3.1.2. Mathematical description of algorithm

a. Asymptotic theory for thick layers

In the case of optically thick layers overlying a Lambertian surface, the expression for the reflection function of a conservative scattering atmosphere can be written as (King 1987)

$$R(\tau_c; \mu, \mu_0, \phi) = R_\infty(\mu, \mu_0, \phi) - \frac{4(1-A_g)K(\mu)K(\mu_0)}{[3(1-A_g)(1-g)(\tau_c+2q_0) + 4A_g]} , \tag{7}$$

from which the scaled optical thickness τ_c' can readily be derived:

$$\tau_c' = (1-g)\tau_c = \frac{4K(\mu)K(\mu_0)}{3[R_\infty(\mu, \mu_0, \phi) - R(\tau_c; \mu, \mu_0, \phi)]} - 2q' - \frac{4A_g}{3(1-A_g)} . \tag{8}$$

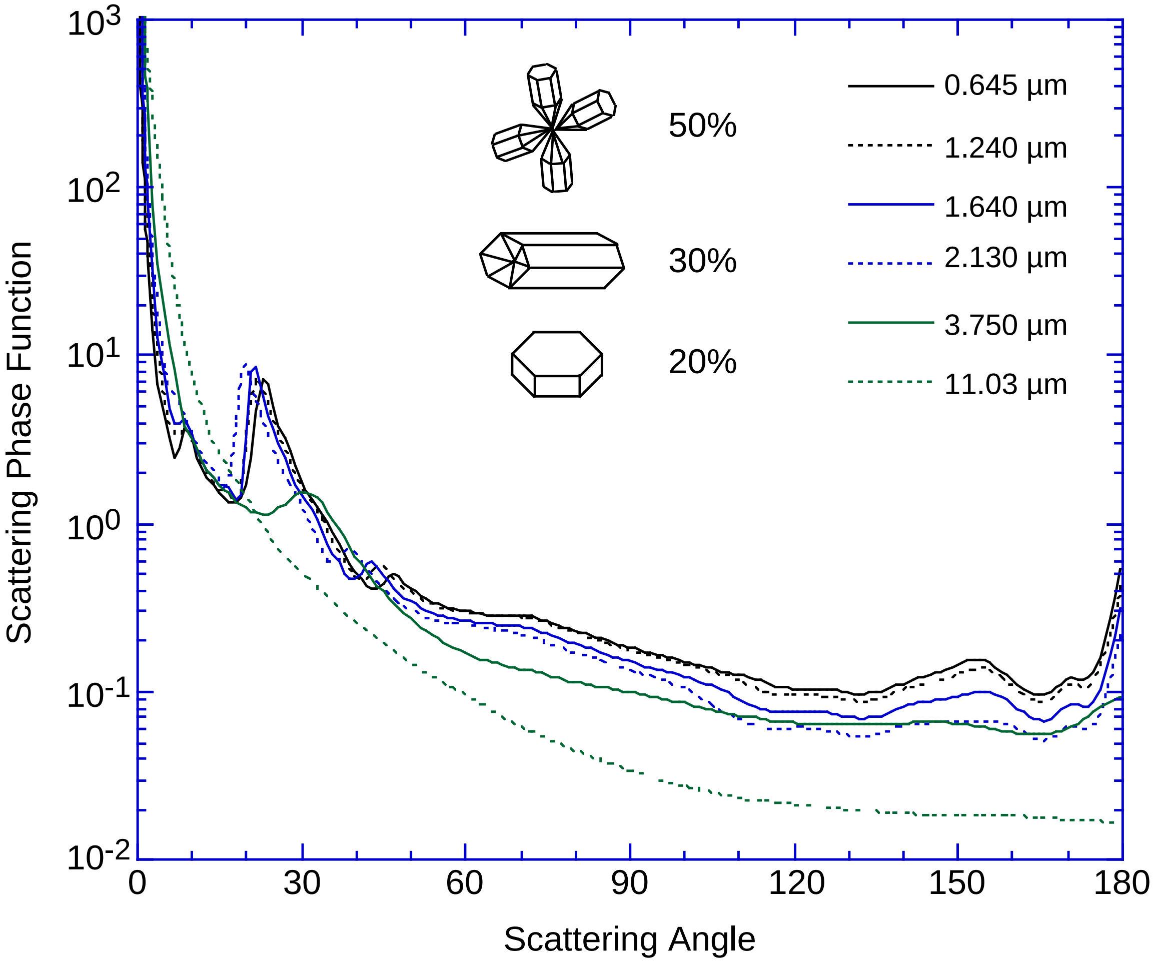

Figure 8. Scattering phase functions for the ice cloud model shown in Fig. 7, calculated for six selected MODIS bands.

In these expressions $R(\tau_c;\ \mu,\ \mu_0,\ \phi)$ is the measured reflection function at a nonabsorbing wavelength, $R_\infty(\mu,\ \mu_0,\ \phi)$ the reflection function of a semi-infinite atmosphere, $K(\mu)$ the escape function, A_g the surface (ground) albedo, g the asymmetry factor, and q_0 the extrapolation length for conservative scattering. The reduced extrapolation length $q' = (1-g)q_0$ lies in the range 0.709 to 0.715 for all possible phase functions (van de Hulst 1980), and can thus be regarded as a constant ($q' \simeq 0.714$).

From Eq. (8) we see that the scaled optical thickness of a cloud depends on q', A_g, $K(\mu)$ and the *difference* between $R_\infty(\mu,\ \mu_0,\ \phi)$ and the measured reflection function. At water-absorbing wavelengths outside the molecular absorption bands (such as 1.64, 2.13 and 3.75 µm), the reflection function of optically thick atmospheres overlying a Lambertian surface can be expressed as (King 1987)

$$R(\tau_c;\, \mu, \mu_0, \phi) \;=\; R_\infty(\mu, \mu_0, \phi) \;-\; \frac{m\left[(1-A_g A^*)l - A_g m n^2\right] K(\mu) K(\mu_0) e^{-2k\tau_c}}{\left[(1-A_g A^*)(1-l^2 e^{-2k\tau_c}) + A_g m n^2 l e^{-2k\tau_c}\right]}\;, \qquad (9)$$

where k is the diffusion exponent (eigenvalue) describing the attenuation of radiation in the diffusion domain, A^* the spherical albedo of a semi-infinite atmosphere, and m, n and l constants. All five asymptotic constants that appear in this expression [A^*, m, n, l and $k/(1-g)$] are strongly dependent on the single scattering albedo ω_0, with a somewhat weaker dependence on g. In fact, van de Hulst (1974, 1980) and King (1981) showed that these constants can be well represented by a function of a similarity parameter s, defined by Eq. (3), where s reduces to $(1 - \omega_0)^{1/2}$ for isotropic scattering and spans the range 0 ($\omega_0 = 1$) to 1 ($\omega_0 = 0$). Similarity relations for the asymptotic constants that arise in Eqs. (7-9) can be found in King et al. (1990), and can directly be computed using eigenvectors and eigenvalues arising in the discrete ordinates method (Nakajima and King 1992).

b. Retrieval example

To assess the sensitivity of the reflection function to cloud optical thickness and effective radius, we performed radiative transfer calculations for a wide variety of solar zenith angles and observational zenith and azimuth angles at selected wavelengths in the visible and near-infrared. Figure 9a (9b) shows representative calculations relating the reflection functions at 0.664 and 1.621 µm (2.142 µm). These wavelengths were chosen because they are outside the water vapor and oxygen absorption bands and yet have substantially different water droplet (or ice particle) absorption characteristics (cf. Fig. 2). These wavelengths correspond to three bands of the MAS, but may readily be adapted to the compa-

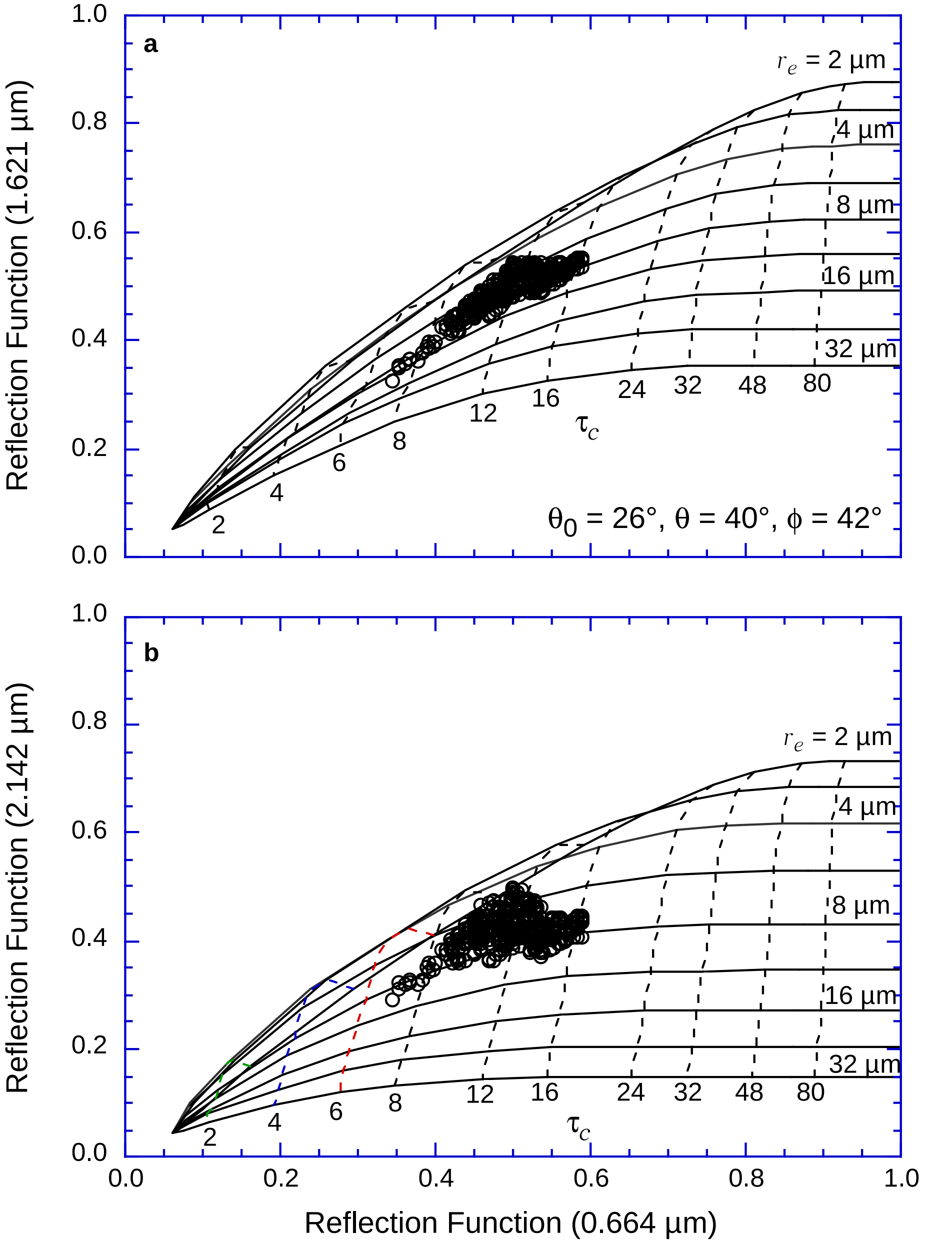

Figure 9. Theoretical relationship between the reflection function at 0.664 and (a) 1.621 µm and (b) 2.142 µm for various values of τ_c (at 0.664 µm) and r_e when θ_0 = 26°, θ = 40° and ϕ = 42°. Data from measurements above marine stratocumulus clouds during ASTEX are superimposed on the figure (22 June 1992).

rable 0.645, 1.64, 2.13 and 3.75 µm bands of MODIS.

Figure 9 clearly illustrates the underlying principles behind the simultaneous determination of τ_c and r_e from reflected solar radiation measurements. The minimum value of the reflection function at each wavelength corresponds to the reflection function of the underlying surface at that wavelength in the absence of an atmosphere. For the computations presented in Fig. 9, the underlying surface was assumed to be Lambertian with $A_g = 0.06$, 0.05, and 0.045 for wavelengths of 0.664, 1.621, and 2.142 µm, respectively, roughly corresponding to an ocean surface. The dashed curves in Fig. 9 represent the reflection functions at 0.664, 1.621 and 2.142 µm that result for specified values of the cloud optical thickness at 0.664 µm. The solid curves, on the other hand, represent the reflection functions that result for specified values of the effective particle radius. These results show, for example, that the cloud optical thickness is largely determined by the reflection function at a nonabsorbing wavelength (0.664 µm in this case), with little dependence on particle radius. The reflection function at 2.142 µm (or 1.621 µm), in contrast, is largely sensitive to r_e, with the largest values of the reflection function occurring for small particle sizes. In fact, as the optical thickness increases ($\tau_c \gtrsim 12$), the sensitivity of the nonabsorbing and absorbing bands to τ_c(0.664 µm) and r_e is very nearly orthogonal. This implies that under these optically thick conditions we can determine the optical thickness and effective radius nearly independently, and thus measurement errors in one band have little impact on the cloud optical property determined primarily by the other band. The previously described multiple solutions are clearly seen as r_e and τ_c decrease.

The data points superimposed on the theoretical curves of Fig. 9 represent over 400 measurements obtained with the MAS, a 50-band scanning spectrometer that was mounted in the right wing superpod of the NASA ER-2 aircraft during ASTEX. These observations were obtained as the aircraft flew over marine stratocumulus clouds in the vicinity of the Azores approximately 1000 km southwest of Lisbon on 22 June 1992.

c. Atmospheric corrections: Rayleigh scattering

As discussed in the previous section, the sensor-measured intensity at visible wavelengths (0.66 µm) is primarily a function of cloud optical thickness, whereas near-infrared intensities (1.6, 2.1, and 3.7 µm) are sensitive both to optical thickness and, especially, cloud particle size. As a consequence, Rayleigh scattering in the atmosphere above the cloud primarily affects the cloud optical thickness retrieval since the Rayleigh optical thickness in the near-infrared is negligible. Because the Rayleigh optical thickness in the visible wavelength region is small (about 0.044 at 0.66 µm), it is frequently overlooked in retrieving cloud optical thickness.

We simplified the air-cloud system as a two-layer atmosphere with molecules above the cloud, and carried out simulations with an adding-doubling code to investigate the Rayleigh scattering effects on cloud optical thickness retrievals. Figures 10a and 10b provide typical errors $\Delta\tau_c$ (%) in retrieved cloud optical thickness τ_c without making any Rayleigh corrections. These errors apply to a cloud with an effective particle radius r_e = 8 µm. Figure 10a applies to errors $\Delta\tau_c$ at different solar and viewing zenith angles when $\tau_c = 2$, whereas Figure 10b pertains to $\Delta\tau_c$ for different solar angles and various cloud optical thicknesses when the viewing zenith angle $\theta = 45.2°$. Figure 10a shows that, for thin clouds, $\Delta\tau_c$ ranges from 15 to 60% for solar and viewing angles ranging from 0-80°. Errors increase with increasing solar and/or viewing angles because of enhanced Rayleigh scattering contributions at large angles. On the other hand, Figure 10b shows that, for thick clouds, $\Delta\tau_c$ can still be as high as 10-60% for solar zenith angles $\theta_0 \geq 60°$. Therefore, it is important to correct for Rayleigh scattering contributions to the reflected signal from a cloud layer both for (i) the case of thin clouds, and (ii) for large solar zenith angles and all clouds.

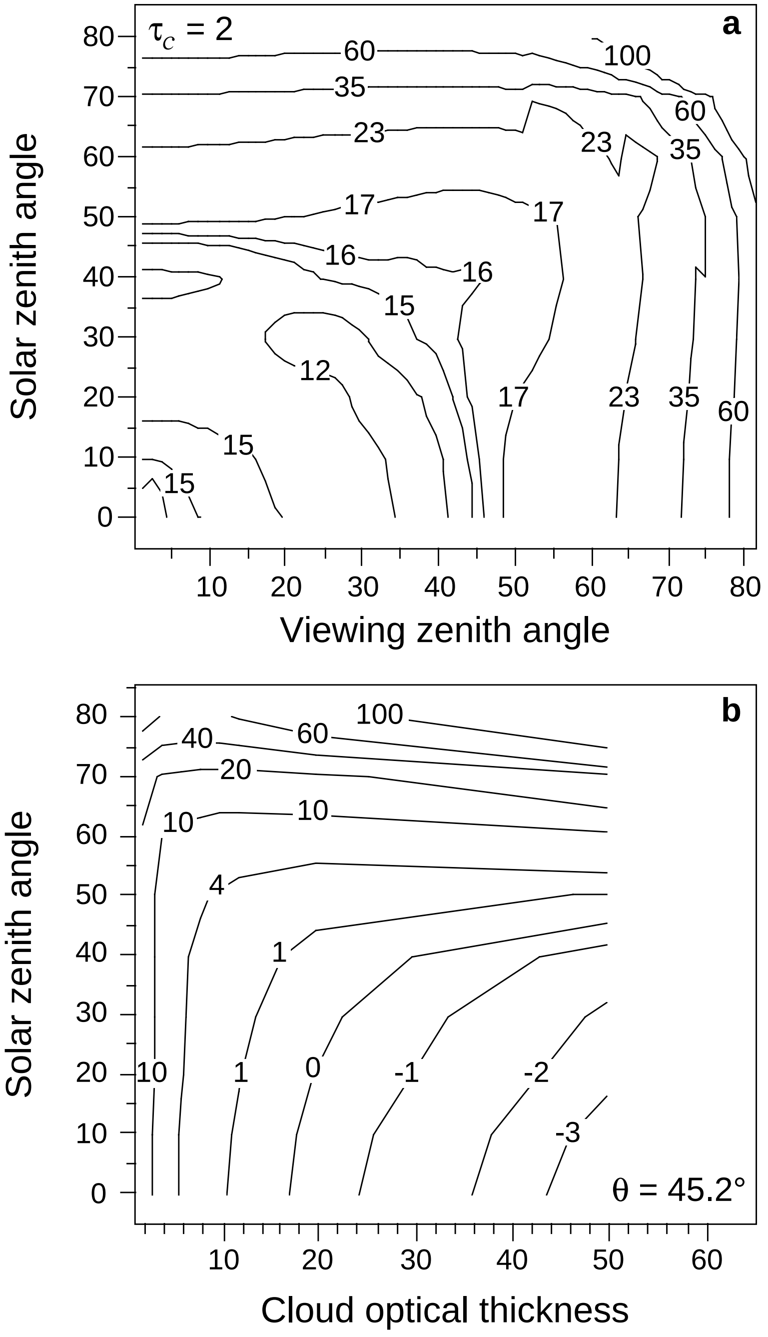

Figure 10. Error $\Delta\tau_c$ (%) in retrieved cloud optical thickness without Rayleigh corrections for (a) $\tau_c = 2$ and (b) $\theta = 45.2°$. The azimuth angle $\phi = 90°$ in both cases.

We developed an iterative method for effectively removing Rayleigh scattering contributions from the measured intensity signal in cloud optical thickness retrievals (Wang and King 1997). In brief, by assuming that no multiple scattering occurs in the Rayleigh layer, we decomposed the sensor-measured upward reflection function of the two-layer air-cloud atmosphere at the top of the atmosphere arising from (i) direct Rayleigh single scattering without reflection from the cloud, (ii) contributions of single interactions between air molecules and clouds, and (iii) reflection of the direct solar beam from the cloud. By removing contributions (i) and (ii) from the sensor-measured reflection function, we were able to derive iteratively the cloud top reflection function in the absence of Rayleigh scattering for use in cloud optical thickness retrievals. The Rayleigh correction algorithm has been extensively tested for realistic cloud optical and microphysical properties with different solar zenith angles and viewing geometries. From simulated results we concluded that, with the proposed Rayleigh correction algorithm, the error in retrieved cloud optical thickness was reduced by a factor of 2 to over 10 for both thin clouds as well as thick clouds with large solar zenith angles. The iteration scheme is efficient and has been incorporated into our cloud retrieval algorithm.

d. Atmospheric corrections: Water vapor

The correlated *k*-distribution of Kratz (1995) can be used to calculate the gaseous atmospheric transmission and/or emission for all MODIS bands. The primary input for this code is an atmospheric temperature and water vapor profile for the above-cloud portion of the atmosphere. It is expected that temperature and humidity can be provided by NCEP, DAO, or MOD07 (for the nearest clear sky pixel), as discussed in Section 3.3.1.b. Alternatively, it may turn out that many of the MODIS bands are not particularly sensitive to the distribution of water vapor, but only to the column amount. For such bands, above-cloud precipitable water estimates from MOD05 may be sufficient. Estimates of ozone amount, from either MOD07 or ancillary sources, will be needed for the 0.645 µm band if standard values prove insufficient.

The effects of the atmosphere need to be removed so that the cloud-top reflectance and/or emission can be determined. It is these cloud-top quantities that are stored in the libraries of Fig. 11 (see below). Ignoring Rayleigh or aerosol scattering, gaseous absorption in the above-cloud atmosphere can be accounted for with the following equation (Platnick and Valero 1995):

$$\begin{aligned} I(\mu, \mu_0, \phi) = {} & I^{\mathrm{solar}}_{\mathrm{clo}ud-\mathrm{top}}(\tau_{\mathrm{c}}, r_e, A_{\mathrm{g}}; \mu, \mu_0, \phi)\, t_{\mathrm{atm}}(\mu)\, t_{\mathrm{atm}}(\mu_0) \\ & + I^{\mathrm{solar}}_{\mathrm{atm}}(\mu, \mu_0, \phi) + I^{\mathrm{emission}}_{\mathrm{clou}\,d-\mathrm{top}}(\tau_{\mathrm{c}}, r_e, A_{\mathrm{g}}; \mu)\, t_{\mathrm{atm}}(\mu) \\ & + I^{\mathrm{emission}}_{\mathrm{atm}}(\mu), \end{aligned} \tag{10}$$

where I is the measured intensity at the top-of-atmosphere, $I_{\mathrm{cloud\text{-}top}}$ is the cloud-top intensity, including surface effects, in the absence of an atmosphere, and t_{atm} is the above-cloud transmittance in either the μ or μ_0 directions. In general, both the cloud and atmosphere contribute emitted (I^{emission}) and solar scattered (I^{solar}) radiant energy. The first term accounts for the effect of the atmosphere on the net cloud-surface reflectance and the third term the effect of cloud and surface emission. For the 3.75 µm band both scattered solar and emitted thermal terms are needed; for shorter wavelength bands, only solar terms are needed; in the thermal infrared, only emission terms are needed.

Though not strictly correct, it is assumed that in practice this gaseous absorption layer can be treated as separate from the Rayleigh scattering layer described above (or any aerosol layer), such that the specific corrections can be applied independently.

e. Technical outline of multi-band algorithm

A generalized schematic description of the cloud retrieval algorithm is given in Figs. 11-13. Figure 11 shows the steps involved in calculating the reflection

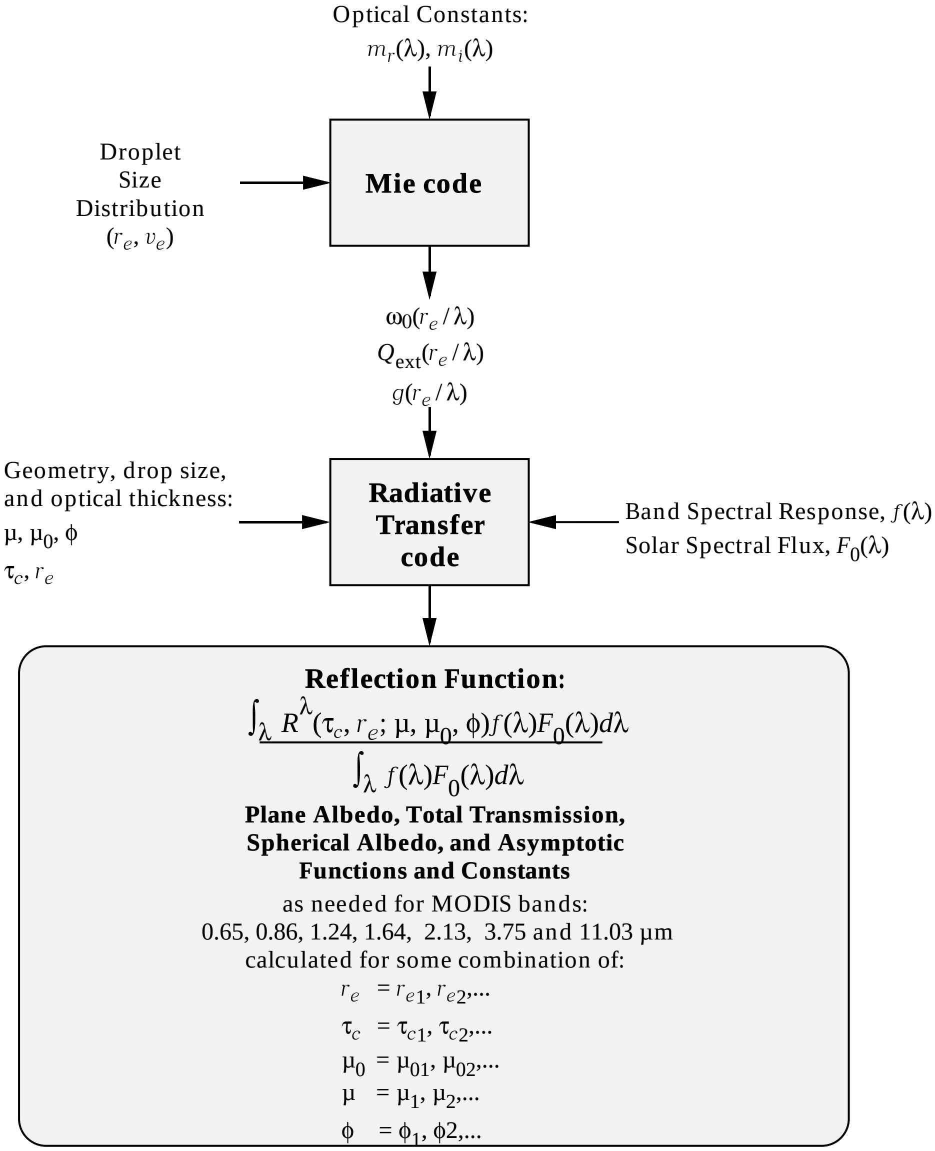

Figure 11. Schematic for generating the reflection function, transmission function, plane albedo, spherical albedo, and asymptotic function parameter library.

function, transmission function, and spherical albedo libraries, including (i) the use of a Mie theory (or nonspherical ice scattering) code for determining optical parameters (ω_0, Q_{ext}, g and/or phase function) from the optical constants of water, and (ii) a radiative transfer code for determining the reflection function, spherical albedo, and asymptotic functions and constants as a function of r_e, τ_c, and geometry.

In computing the optical constants for liquid water, we used complex refractive indices tabulated by Hale and Querry (1973) for wavelengths in the range $0.25 \le \lambda \le 0.69$ µm, Palmer and Williams (1974) for $0.69 < \lambda \le 2.0$ µm, and Downing and Williams (1975) for $\lambda > 2.0$ µm. The natural log-normal size distribution for water droplets was used for all computations with an effective variance $v_e = 0.13$. The influence of surface reflectance is calculated by assuming that the cloud is vertically homogeneous with a surface that reflects radiation according to Lambert's law with ground albedo A_g as

$$\begin{aligned} R(\tau_\mathrm{c}, r_e; \mu, \mu_0, \phi) &= R_\mathrm{cloud}(\tau_\mathrm{c}, r_e; \mu, \mu_0, \phi) \\ &+ \frac{A_g}{1 - A_g \bar{r}_\mathrm{cloud}(\tau_c, r_e)} t_\mathrm{cloud}(\tau_\mathrm{c}, r_e; \mu)\, t_\mathrm{cloud}(\tau_\mathrm{c}, r_e; \mu_0), \qquad (11) \end{aligned}$$

where $R_\mathrm{cloud}(\tau_\mathrm{c}, r_e; \mu, \mu_0, \phi)$, $t_\mathrm{cloud}(\tau_\mathrm{c}, r_e; \mu_0)$, and $\bar{r}_\mathrm{cloud}(\tau_\mathrm{c}, r_e)$ are, respectively, the reflection function, total transmission (diffuse plus direct), and spherical albedo of a cloud layer when $A_g = 0$. Eq. (11) simplifies the computations of $R(\tau_\mathrm{c}, r_e; \mu, \mu_0, \phi)$ for different surface types with lookup libraries of $R_\mathrm{cloud}(\tau_\mathrm{c}, r_e; \mu, \mu_0, \phi)$, $t_\mathrm{cloud}(\tau_\mathrm{c}, r_e; \mu_0)$, and $\bar{r}_\mathrm{cloud}(\tau_\mathrm{c}, r_e)$ for various cloud microphysical and optical properties and for different solar and viewing geometries.

The asymptotic functions and constants that appear in Eqs. (7)-(9) can readily be determined either following radiative transfer computations, using the asymptotic fitting method of van de Hulst (1980), or directly from the Mie code using the coefficients of the Legendre polynomial expansion of the phase function, as described by Nakajima and King (1992).

Figure 12 shows an algorithm for retrieving τ_c and r_e from comparisons of measured reflection functions with entries in the library. The definition of the residual used for determining the best fit is typically defined as a least-squares fit, and is often a weighted fit (Twomey and Cocks 1989).

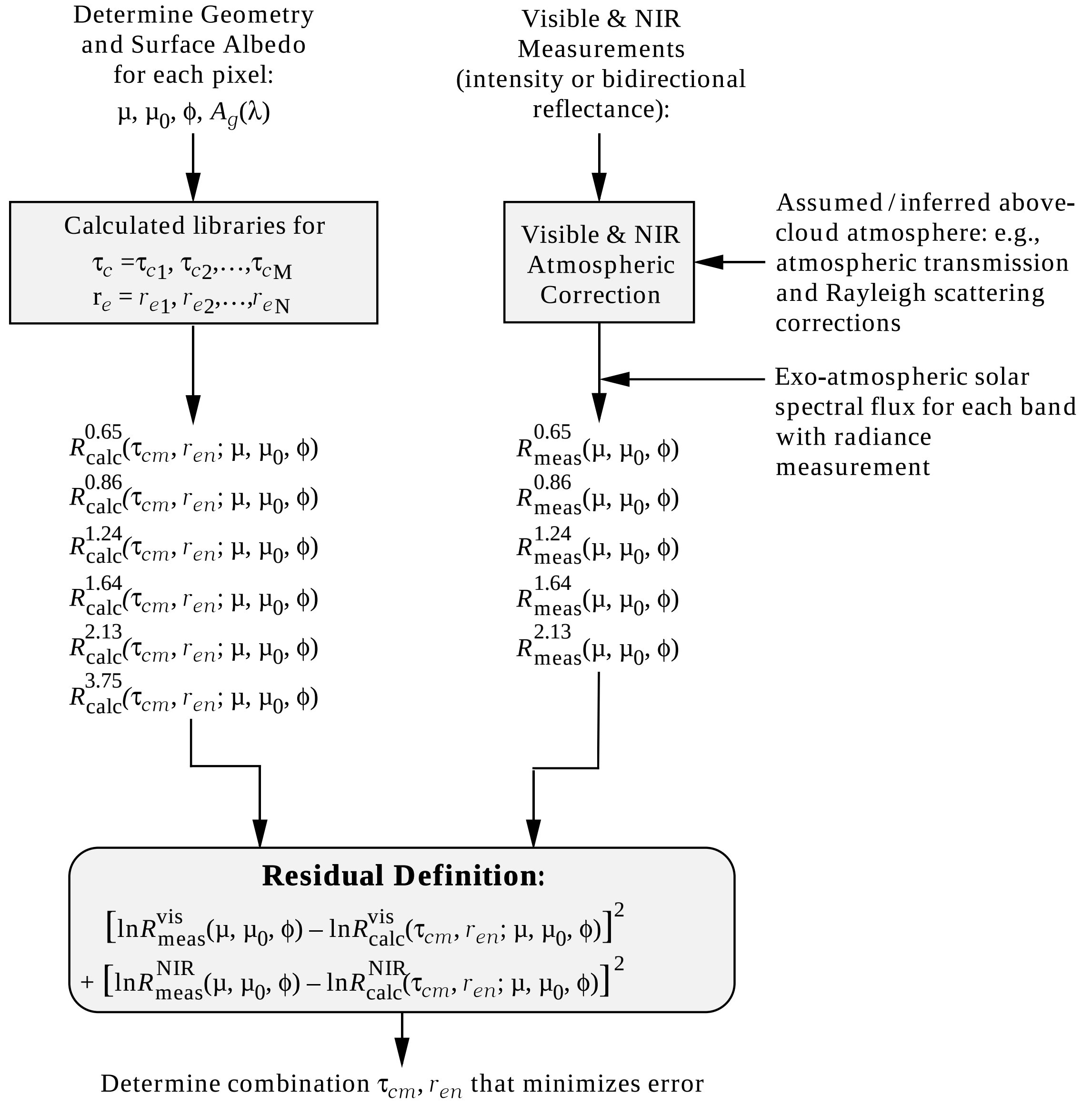

Figure 12. A general cloud retrieval algorithm for determining best fit for τ_c and r_e in the 0.65, 1.64 and 2.13 µm bands.

The use of the 3.75 µm band complicates the algorithm because radiation emitted by the cloud is comparable to, and often dominates, the solar reflectance. Cloud emission at 3.75 µm is weakly dependent on r_e, unlike solar reflectance (cf. Fig. 4), so the relative strength of the two depends on particle size. Surface emission can also be significant for thin clouds ($\tau_c \lesssim 5$). For example, with cloud and surface temperatures of 290 K, emission and reflectance are approximately equal for r_e = 10 µm (Platnick and Twomey 1994). An assumption that is often made is that clouds are isothermal. Retrievals using this band include those made by Arking and Childs (1985), Grainger (1990), Platnick (1991), Kaufman and Nakajima (1993), Han et al. (1994, 1995), Platnick and Valero (1995), and Nakajima and Nakajima (1995), all of whom used the visible and 3.7 µm bands of AVHRR.

To correct for thermal emission in the 3.75 µm band, we decomposed the total upward reflection function at the top of the atmosphere into solar, thermal, and surface contributions. Ignoring atmospheric effects above the cloud, which can readily be corrected as described above for both water vapor and Rayleigh scattering effects, we can write the total above-cloud measured reflection function as (Platnick and Valero 1995; Nakajima and Nakajima 1995)

$$\begin{aligned} R_{\mathrm{meas}}(\tau_{\mathrm{c}}, r_e; \mu, \mu_0, \phi) &= R_{\mathrm{cloud}}(\tau_{\mathrm{c}}, r_e; \mu, \mu_0, \phi) \\ &+ \frac{A_g}{1 - A_g \bar{r}_{\mathrm{cloud}}(\tau_c, r_e)} t_{\mathrm{cloud}}(\tau_{\mathrm{c}}, r_e; \mu)\, t_{\mathrm{cloud}}(\tau_{\mathrm{c}}, r_e; \mu_0) \\ &+ \varepsilon^*_{\mathrm{cloud}}(\tau_{\mathrm{c}}, r_e; \mu)\, \mathrm{B}(T_c) \frac{\pi}{\mu_0 F_0} + \varepsilon^*_{\mathrm{surface}}(\tau_{\mathrm{c}}, r_e; \mu)\, \mathrm{B}(T_g) \frac{\pi}{\mu_0 F_0}. \end{aligned} \tag{12}$$

In this equation, the first two terms account for solar reflectance and are identical to Eq. (11), $\varepsilon^*_{\mathrm{surface}}(\tau_{\mathrm{c}}, r_e; \mu)$ is the effective surface emissivity that includes the effect of the cloud on radiation emitted by the surface, and $\varepsilon^*_{\mathrm{cloud}}(\tau_{\mathrm{c}}, r_e; \mu)$ is the effective cloud emissivity that can be formulated to include cloud emission that is reflected by the surface. These emissivities are given by

$$\begin{aligned} \varepsilon^*_{\mathrm{cloud}}(\tau_{\mathrm{c}}, r_e; \mu) &= [1 - t_{\mathrm{cloud}}(\tau_{\mathrm{c}}, r_e; \mu) - r_{\mathrm{cloud}}(\tau_{\mathrm{c}}, r_e; \mu)] \\ &\quad + \text{ surface interaction terms}, \end{aligned} \tag{13}$$

$$\varepsilon^*_{\mathrm{surface}}(\tau_{\mathrm{c}}, r_e; \mu) = \frac{1 - A_g}{1 - A_g \bar{r}_{\mathrm{cloud}}(\tau_c, r_e)} t_{\mathrm{cloud}}(\tau_{\mathrm{c}}, r_e; \mu), \tag{14}$$

where $r_{\mathrm{cloud}}(\tau_{\mathrm{c}}, r_e; \mu)$ is the plane albedo of the cloud, and $\mathrm{B}(T_c)$ and $\mathrm{B}(T_g)$ are, respectively, the Planck function at cloud top temperature T_c and surface temperature T_g.

The terms on the right-hand side of Eq. (12) pertain, in turn, to (i) solar reflection by the cloud in the absence of surface reflection, (ii) contributions from multiple reflection of solar radiation by the Earth's surface, (iii) thermal emission from the cloud, and (iv) thermal emission from the surface. For thin clouds ($\tau_c \lesssim 5$), the second and fourth terms dominate, with surface emission contributing over 50% of the total measured intensity. For thick clouds ($\tau_c > 10$), on the other hand, the first and third terms are the most important. The surface interaction terms in the effective cloud emissivity account for downward emitted cloud radiation reflected by the surface and back through the cloud. This is generally insignificant except for perhaps the optically thinnest clouds. The cloud top temperature T_c can be obtained either as an output of Menzel and Strabala's (1997) MODIS cloud top property algorithm or from output of the Data Assimilation Office algorithm (DAO 1996), as discussed in Section 3.3.1.b. Surface temperature T_g is also required under cloudy conditions, and we intend to obtain this parameter from various sources, depending on whether the pixel is over land or water (cf. Section 3.3.1.b). This is only a serious problem for optically thin (i.e., cirrus) clouds.

The thermal emission from the atmosphere above the cloud [the fourth term in Eq. (10)] is usually of second order importance, contributing only a few percent to the total intensity. This emission can be expressed as

$$R_{\mathrm{atm}}(\mu) = -\frac{\pi}{\mu_0 F_0} \int_0^{p_0} B(T(p))\ \mathrm{d}t_{\mathrm{atm}}(p;\ \mu), \tag{15}$$

$$\approx \frac{\pi}{\mu_0 F_0} \left[1 - t_{\mathrm{atm}}(\mu)\right] \mathrm{B}(T_a), \tag{16}$$

where p_0 is the cloud top pressure and T_a is an appropriate atmospheric temperature. For a given temperature and moisture profiles, either obtained from Menzel and Gumley's (1997) MODIS atmospheric profiles product (cf. Fig. 1), or from an NCEP or DAO gridded data set, we can calculate the $R_{\mathrm{atm}}(\mu)$ term using Eq. (15). An alternative approach is to use Eq. (16) with a given total water-vapor loading above the cloud and some averaged atmospheric temperature. This probably will be accurate enough because of relatively small thermal contributions from the atmosphere. By removing the thermal contributions (the third and fourth terms) from the sensor-measured intensity, the 3.75 µm algorithm operates in a manner quite similar to that for the 1.64 and 2.13 µm bands.

We plan on utilizing Nakajima and King's (1990) algorithm for retrieving the cloud optical thickness and effective radius using the 1.64 and 2.13 µm bands, together with a similar algorithm based on Platnick (1991) and Nakajima and Nakajima (1995) for removing the thermal contributions from the 3.75 µm band, as outlined above and in Figure 13.

f. Retrieval of cloud optical thickness and effective radius

In the description of the algorithm that follows, all subsequent references to τ_c will be scaled, or normalized, to an optical thickness at 0.65 µm (or $2/Q_{\mathrm{ext}}(r_e/\lambda)$, used previously in Fig. 5). In order to implement the Nakajima and King algorithm, it is first necessary to compute the reflection function, plane albedo, total transmission, and spherical albedo for the standard problem of plane-parallel homogeneous cloud layers (A_g) with various τ_c' and $r_e = 2^{(n+1)/4}$ for $n = 5, \cdots, 19$, assuming a model cloud particle size distribution such as a log-normal size distribution. We have generated the reflection function libraries for $\tau_c' = 0.4$, 0.8, 1.2 and ∞ ($\tau_c = 3$, 5, 8 and ∞), flux libraries for $\tau_c' = 0.4$, 0.8, and 1.2, and a library for asymptotic functions and constants. These values of τ_c' are selected such that interpolation errors are everywhere ≤ 3% for $\tau_c' \geq 0.6$ ($\tau_c \simeq 4$). This was

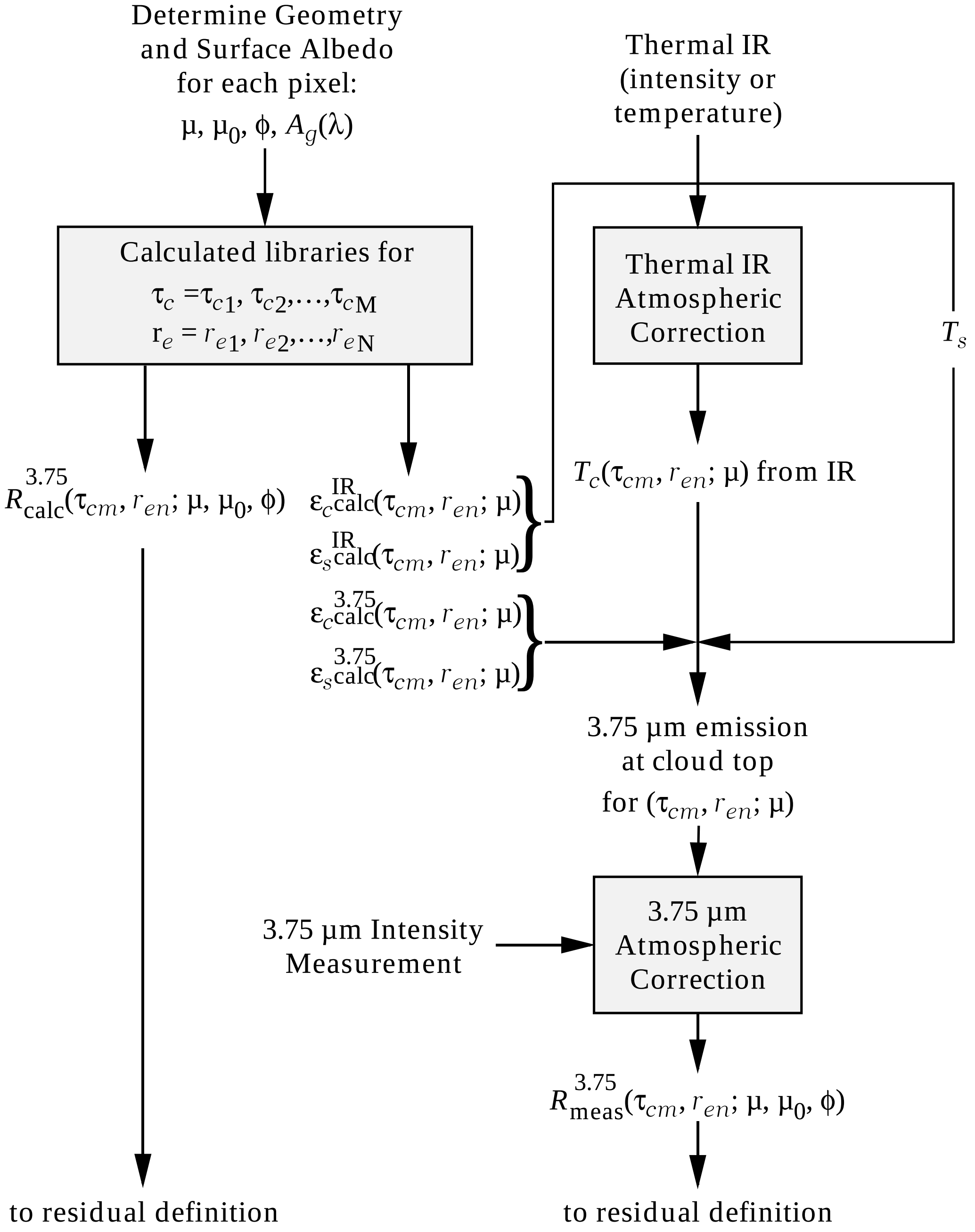

Figure 13. A general cloud retrieval algorithm for determining best fit for τ_c and r_e in the 3.75 µm band.

accomplished using a combination of asymptotic theory for $\tau_c' \geq 1.8$ ($\tau_c \simeq 12$) and spline under tension interpolation for $\tau_c' < 1.8$.

The interpolation scheme reduces the number of library optical thickness entries substantially, but replaces those entries with a combination of spline interpolation and asymptotic formulae, depending on optical thickness. Calculations of the reflection function can be performed using the discrete ordinates method formulated by Nakajima and Tanaka (1986) or Stamnes et al. (1988). The asymptotic functions and constants that appear in Eqs. (7)–(9) can be obtained from solutions of an eigenvalue equation that arises in the discrete ordinates method (Nakajima and King 1992).

If one assumes that each reflection function measurement is made with equal relative precision, maximizing the probability that $R^i_{\mathrm{meas}}(\mu, \mu_0, \phi)$ observations have the functional form $R^i_{\mathrm{calc}}(\tau_c, r_e; \mu, \mu_0, \phi)$ is equivalent to minimizing the statistic χ^2, defined as (Nakajima and King 1990)

$$\chi^2 = \sum_i \left[\ln R^i_{\mathrm{meas}}(\mu, \mu_0, \phi) - \ln R^i_{\mathrm{calc}}(\tau_c, r_e; \mu, \mu_0, \phi)\right]^2 , \qquad (17)$$

where the summation extends over all wavelengths λ_i for which measurements have been made and calculations performed.

Minimizing χ^2 as defined by Eq. (17) is equivalent to making an unweighted least-squares fit to the data (Bevington 1969). The minimum value of χ^2 can be determined by setting the partial derivatives of χ^2 with respect to each of the coefficients [τ_c(0.65 or 0.75 µm), r_e] equal to zero. Due to the complicated dependence of the reflection function on τ_c and r_e, however, this solution is nonlinear in the unknowns τ_c and r_e such that no analytic solution for the coefficients exists. Even for optically thick layers, where asymptotic theory applies, $R^i_\infty(r_e; \mu, \mu_0, \phi)$ is a complicated function of the phase function, and hence r_e, as King (1987) has shown by deriving the cloud optical thickness assuming the clouds had two different phase functions but the same asymmetry factor.

In order to solve this nonlinear least-squares problem, we have adopted a procedure whereby the scaled optical thickness τ_c', and hence τ_c and g, is determined as a function of r_e from a reflection function measurement at 0.75 µm (or bands 1, 2, or 5 for the case of MODIS data). For $\tau_c' < 1.8$ we used spline under tension interpolation (Cline 1974) of reflection function calculations $R^i_{\text{calc}}(\tau_c, r_e; \mu, \mu_0, \phi)$, and for $\tau_c' \geq 1.8$ we used Eq. (8), as described by King (1987). Having determined an array of possible solutions $[\tau_c, r_e]$, it is straightforward to calculate χ^2 as a function of r_e using measurements and calculations for one or more additional bands. Thus the determination of the optimum values of τ_c and r_e becomes a nonlinear least-squares problem in only one unknown r_e, since τ_c is given uniquely from a knowledge of r_e. The only subtlety worth noting is that it is essential to allow for the spectral dependence of $\tau_c(\lambda)$ and $A_g(\lambda)$ when interpolating radiative transfer calculations $[\tau_c'(\lambda) < 1.8]$ or applying Eq. (9) $[\tau_c'(\lambda) \geq 1.8]$ at bands other than 0.65 µm.

As an illustration of how this procedure works, Nakajima and King (1990) constructed the χ^2 hypersurface in coefficient space for various combinations of bands. These results, presented in Fig. 14, are based on simulated spherical albedo measurements at (a) 0.75 and 2.16 µm, (b) 0.75, 1.65 and 2.16 µm, (c) 0.75 and 3.70 µm, and (d) 0.75, 1.65, 2.16 and 3.70 µm. The solid curves represent constant values of χ^2. The parameters τ_c and r_e that give the best fit of the measurements R^i_{meas} to the nonlinear function $R^i_{\text{calc}}(\tau_c, r_e)$ are determined by the location of the minimum value of χ^2 in this two-dimensional space. The results presented in Fig. 14 were constructed for the optimum values $\tau_c = 8$ and $r_e = 6$ µm. Searching this hypersurface for the parameters that minimize χ^2 is greatly facilitated by first solving for τ_c as a function of r_e using the reflection function measurement at 0.75 µm. These optical thickness values, shown in each panel of Fig. 14 as a dashed line, must necessarily pass through the absolute minimum of the function χ^2 (assuming no error in the visible measurement). The previously

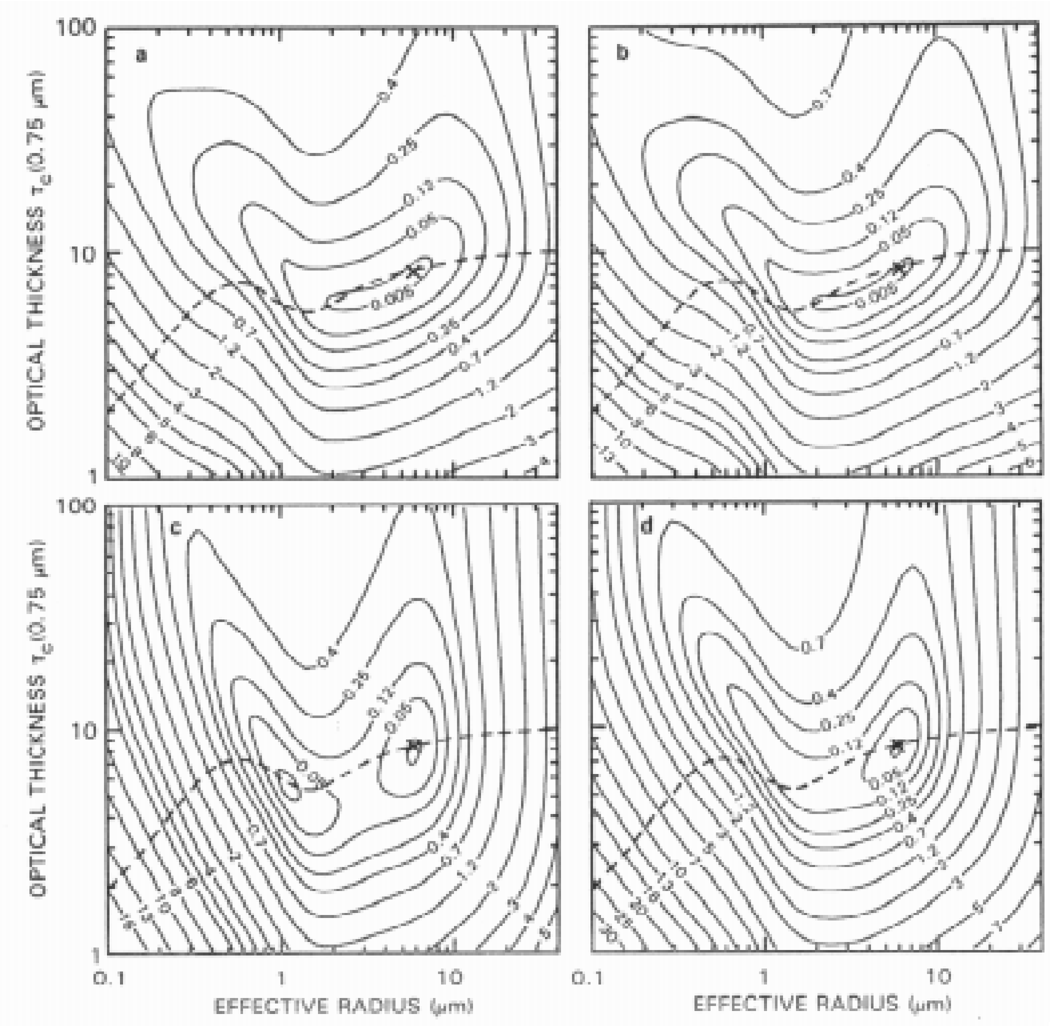

Figure 14. χ^2 hypersurface for theoretically generated spherical albedo measurements at (a) 0.75 and 2.16 µm, (b) 0.75, 1.65 and 2.16 µm, (c) 0.75 and 3.70 µm, and (d) 0.75, 1.65, 2.16 and 3.70 µm. The solid curves represent constant values of χ^2, while the dashed curve in each panel represents the array of possible solutions for $R^{0.75}_{\mathrm{meas}} = 0.495$. These results were constructed for a model cloud layer having $\tau_c(0.75\ \mu\mathrm{m}) = 8$ and $r_e = 6$ µm, located by the minimum value of χ^2 in this two-dimensional space [from Nakajima and King (1990)].

mentioned multiple solutions are readily seen for small τ_c and r_e, though the ambiguity is eliminated in Fig. 14d when using all available near-infrared bands.

We are currently retrieving τ_c and r_e separately using pairs of bands, an appropriate optical thickness-sensitive band, together with an appropriate near-infrared band (e.g., vis and 1.64 µm, vis and 2.13 µm, and vis and 3.75 µm), since each near-infrared band is sensitive to the effective radius at a different depth within the cloud (Platnick 1997). The lowest (optical thickness-sensitive) band will be either 0.65 µm over land, 0.86 µm over water, or 1.24 µm over snow and sea ice surfaces. For water clouds, the effective radius typically increases from cloud base to cloud top, with the 3.75 µm retrieval being the most sensitive to drops high in the cloud and 1.64 µm much lower in the cloud. For ice clouds, the vertical profile of effective radius is just the opposite, with the smallest crystals highest in the cloud. Although the χ^2 multi-band retrieval algorithm described above has the merit of eliminating multiple solutions, the effective radius thus obtained in realistic, vertically inhomogeneous clouds, is some compromise in effective radius. We are thus doing multiple retrievals using the similarity (or differences) in the retrieved results as a quality control indicator in the output data product (cf. Table 5). If the differences between retrievals are excessively large (i.e., $\Delta r_e \gtrsim$ 2 µm), then we will switch to an ice retrieval algorithm that is identical to the one outlined above, but with an ice crystal phase function rather than water droplet phase function in the look-up tables.

3.2. Variance and uncertainty estimates

The overall uncertainties in determining the cloud optical thickness and effective radius can loosely be categorized as originating in either the *model* used for developing the cloud reflection function and emittance libraries, or in the *physical* uncertainties brought about through changing instrument error and atmospheric effects. Though it is difficult to draw the line between the two, it is convenient to consider the model uncertainties to have their source in the library generating algorithm shown schematically in Fig. 11 and the algorithm used for approximating emitted thermal radiation at 3.75 µm. The physical uncertainties can be largely ascribed to the atmospheric correction boxes and the measured data shown in Fig. 12.

3.2.1. Model uncertainties

Several sources of model error are potentially significant. First of all, the treatment of the wavelength integration over the bandpass filters is important because it impacts calculations of the spectral reflection functions and emissivities. Ideally, the spectral integration should be based on the variability of the optical constants across the bandpass filter. For example, the absorption of liquid water, as measured by the imaginary part of the complex refractive index of water, varies significantly throughout the near-infrared wavelength region, whereas the real part of the refractive index is approximately constant over this region. Mie calculations are dependent on the size parameter ($2\pi r/\lambda$), thereby adding another wavelength dependence. For computational reasons, it is desirable to determine the minimum number of wavelengths needed in any retrieval.

In order to assess the impact of finite bandpass characteristics of the MODIS bands on our cloud retrieval algorithm, we performed calculations of the reflection function using 11 equally-spaced wavelengths for each band. These results were then compared with reflection function computations based on a single wavelength at the bandpass center. Ultimately, however, it is the effect of the wavelength integration on the retrieval of τ_c and r_e that is important, not the absolute changes in the reflection functions themselves. Since the near-infrared reflection functions are more sensitive to the finite bandpass characteristics of MODIS, we restrict our analysis to the retrieval of r_e.

Figure 15 shows the error in the retrieval of r_e when using a single wavelength calculation for the 2.14 µm band of MAS, where the 11 wavelength integration over the bandpass characteristics of the band is taken as the “true solution.” The optical thickness is such that the asymptotic reflection function has been reached for most radii. This choice of optical thickness gives a conservative

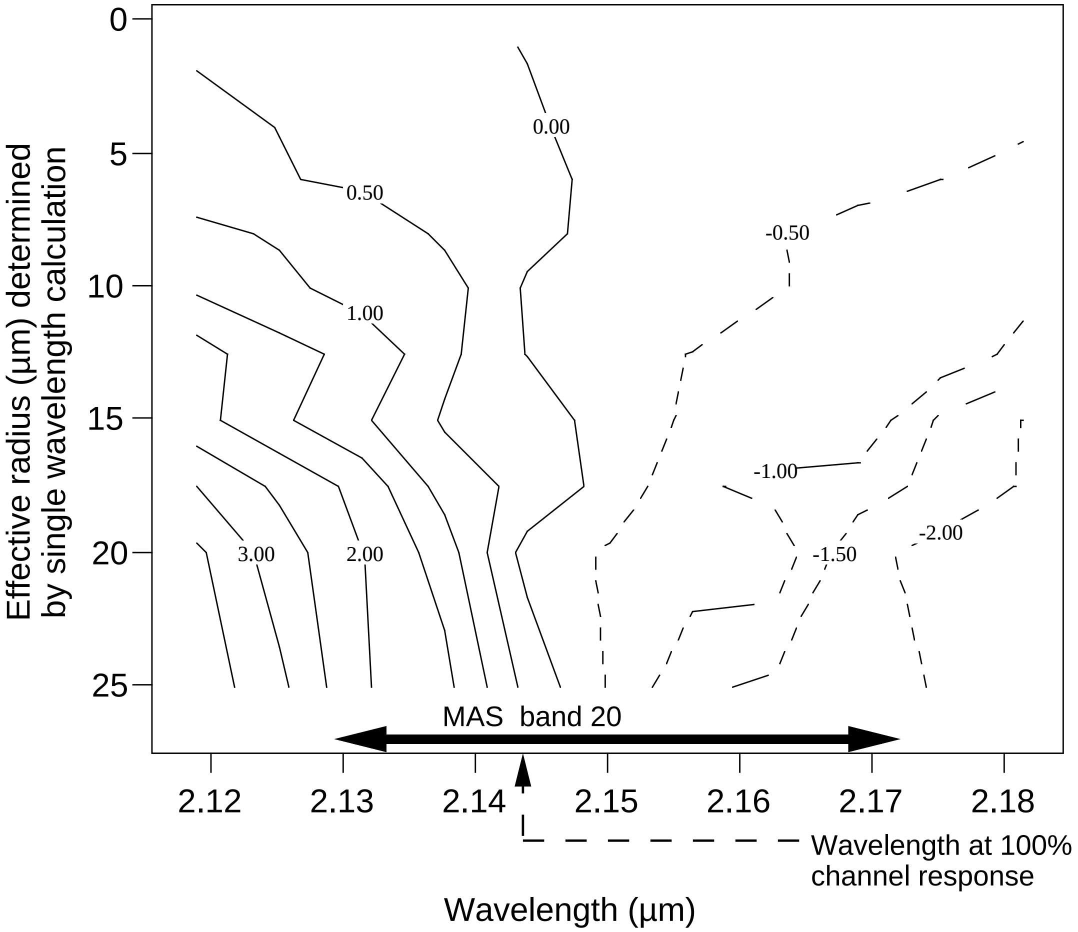

Figure 15. Error in the retrieval of r_e (µm) between (i) using spectrally averaged reflection functions, sensor and solar weighted with 11 wavelengths, and (ii) a single wavelength calculation. These results apply to the MAS 2.14 µm band with $\mu_0 = 0.75$, $\mu = 0.95$, $\tau_c = 50$, and the optical constants of Irvine and Pollack (1968).

estimate of retrieval error since the sensitivity of r_e to reflection function is the smallest. Figure 15 shows that using the wavelength of the peak of the spectral bandpass is sufficient for obtaining effective radii errors within 0.5 µm.

Another approach one might take is to spectrally integrate the optical parameters ω_0^λ, Q_{ext}^l, and g^λ over wavelength and use these results for a single wavelength retrieval. This comparison is shown in Fig. 16 for the same MAS band as shown in Fig. 15. For $\tau_c = 50$, the error is less that 0.1 µm for the expected range of effective radii to be encountered in terrestrial clouds. For an optically thin cloud ($\tau_c = 1$) the error increases to 0.3 µm at $r_e = 4$ µm. However, for such an optically thin cloud, uncertainties in surface reflectance and atmospheric corrections are likely to dominate this error. Similar results were obtained when analyzing MAS 1.62 and 3.73 µm bands. At this time, it appears that an integration over ω_0^λ, Q_{ext}^l, and g^λ will provide an adequate reflectance library. Table 3 summarizes the maximum retrieval errors in r_e for all near-infrared bands (based on calculations at μ_0 = 0.95, 0.75, 0.5, μ = 0.95 and τ_c = 1, 5, 50). Effects of spectral integration on emission in the 3.7 µm bands are not included in Table 3.

The effect of a shift in the central wavelength of the near-infrared bands can also be assessed. For each band, the reflection function changes arising from a

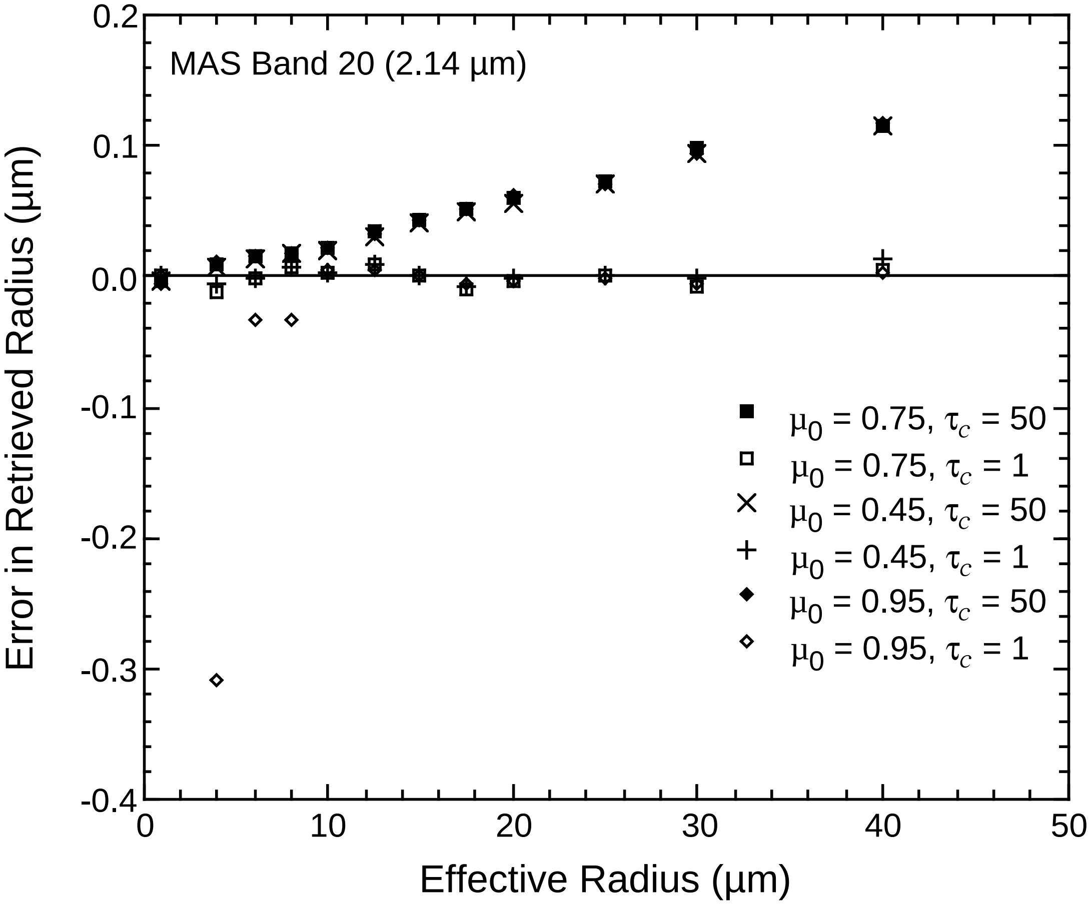

Figure 16. Error in the retrieval of r_e (µm) between (i) using spectrally averaged reflection functions, sensor and solar weighted with 11 wavelengths, and (ii) using reflection function calculations based on spectral averages of cloud optical properties (ω_0^λ, Q_{ext}^λ, and g^λ). These results were obtained using the MAS 2.14 µm band with μ = 0.95 and the optical constants of Irvine and Pollack (1968).

shift of 13% in the bandpass center were compared with those based on spectral integration over the full-width half maximum (FWHM) bandpass of each band (one wavelength increment in the 11 wavelength calculation). Such a spectral shift is approximately equal to the tolerance listed in the MODIS specifications. The effect of a spectral shift on the retrieval of r_e is shown in Fig. 17 for the MAS 2.14 µm band. In general, the error increases with increasing r_e, but for $r_e < 20$ µm the error $\Delta r_e < 0.5$ µm. Table 3 summarizes errors in r_e arising from spectral shifts in other near-infrared bands of MAS and AVHRR. The effect of spectral

Table 3. Summary of approximate maximum error in retrieving effective radius (µm) for MAS near-infrared bands and AVHRR band 3. Calculated for $\mu = 0.95$ and μ_0 variable. For the spectral and optical constant analysis, the two rows for each band correspond to the maximum error as r_e varies from 5 to 20 µm with τ_c variable. For the sensor error analysis, for each band correspond to different optical thicknesses and $5 \le r_e \le 15$ µm. See text for details.

Band	r_e	$\langle R^{\lambda} \rangle - R^{\langle \mathrm{Mie} \rangle}$	$+\lambda_c$ shift (+13% of BW)	$-\lambda_c$ shift (–13% of BW)	r_e(IP) – r_e (PW)*	τ_c	Errors due to sensor intensity or reflectance error			
							±1%	±2%	±5%	±10%
MAS 10 (1.62 µm)	5	+0.09	–0.10	+0.10	+0.5	5	∓ 0.7	∓ 1.3	–3 / +4	+6 / +9
	20	–0.05	–0.55	+0.55	+3.0	50	∓ 0.7	∓ 1.3	∓ 2.7	–4.5 / +6
MAS 20 (2.14 µm)	5	+0.10	–0.15	+0.15	+0.5	5	∓ 0.4	∓ 0.7	∓ 2.0	–3.5 / +4.5
	20	–0.30	–0.50	+0.50	+2.6	50	∓ 0.3	∓ 0.6	∓ 1.4	∓ 2.7
MAS 32† (3.73 µm)	5	+0.25	–0.30	+0.30		5	∓ 0.15	∓ 0.2	∓ 0.6	∓ 1.2
	20	–0.05	–0.70	+0.70		50	∓ 0.2	∓ 0.3	∓ 0.7	–1.4 / +1.7
AVHRR 3 (3.75 µm)	5	+0.45	–0.30	+0.50		5	Same as for MAS 32			
	20	–0.10	–0.70	+1.20		50				

* Difference in retrieved droplet effective radius using reflectance libraries calculated with the optical constants given by IP (Irvine and Pollack 1968) and PW (Palmer and Williams 1974). These computations apply to the case when $\tau_c = 50$.

† Designated as MAS 31 prior to June 1995.

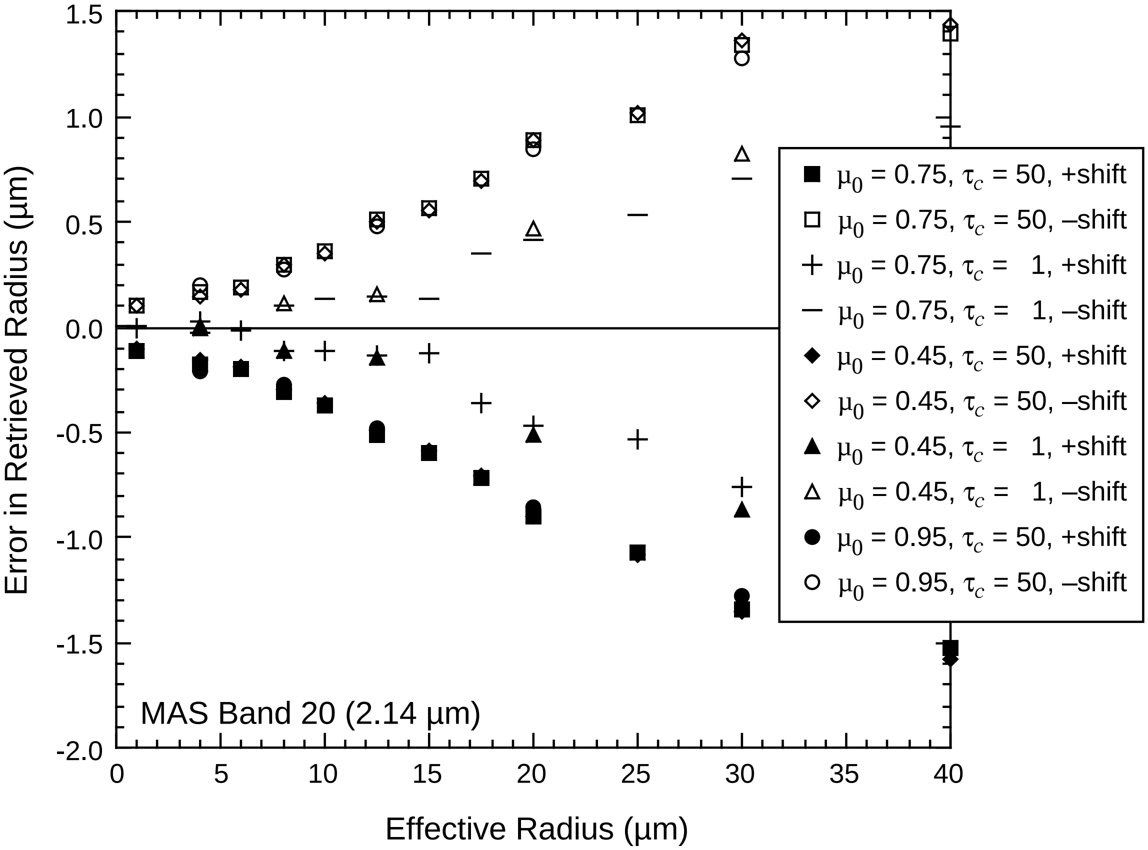

Figure 17. Error in the retrieval of r_e (µm) between (i) using spectrally averaged reflection functions, sensor and solar weighted with 11 wavelengths, and (ii) using reflection function calculations with a spectral shift of 13% (±6.25 nm) in the band's central wavelength These results were obtained using the MAS 2.14 µm band with µ = 0.95 and the optical constants of Irvine and Pollack (1968).

shift on emission is not included in Table 3 for either the MAS or AVHRR 3.7 µm bands.

The optical constants of liquid water are the starting point for all calculations. The optical constants of water in various near-infrared spectral regions are reported in the compilation papers of Irvine and Pollack (1968) and Hale and Querry (1973), and the measurements of Robertson and Williams (1971), Palmer and Williams (1974), Downing and Williams (1975), and Kou et al. (1993). All constants were derived for water at room temperature, with the exception of Kou et al. who also made measurements of supercooled water at -8°C. For the 3.7 µm band, the data of Downing and Williams and Kou et al. agree quite well with those of Irvine and Pollack. In the 1.64 and 2.13 µm bands, on the other hand, differences of up to 11-14% occur between the absorption coefficient of liquid water reported by Irvine and Pollack and corresponding measurements reported by Palmer and Williams, depending on wavelength. The room temperature absorption measurements of Kou et al. are within a few percent of Palmer and Williams. However, absorption bands for their supercooled measurements are slightly shifted toward longer wavelengths giving an increase in absorption over the room temperature values by about 20% at the center of the MODIS 1.64 µm band, and 5% for the 2.13 µm band.

At large cloud optical thicknesses, it can be shown that the fractional effective radius retrieval error is approximately equal, but of opposite sign, to the fractional error in the absorption constant (Platnick and Valero 1995). That is, a library calculated using an absorption constant that is 10% too small would result in a retrieved effective radius that is about 10% too large. Exact calculations of the effects of different absorption coefficients on the retrievals of r_e are shown in Fig. 18 for the 1.62 and 2.14 µm bands of MAS, using both Irvine and Pollack (1968) and Palmer and Williams (1974) data. These results were obtained for several values of optical thickness and solar zenith angle. Note that the fractional effective radius retrieval error is indeed approximately constant with effective radius for the larger optical thicknesses, as mentioned above. A supercooled water cloud (Kou et al. 1993) would show even greater differences. Since it is difficult to know which authors have presented the more accurate liquid water absorption values, the example of Fig. 18 should be regarded as a fundamental uncertainty in the retrieval of effective radius. For computing the libraries of Fig. 11, we have chosen to use the optical constants of Palmer and Williams (1974) for the 1.64 µm MODIS band, and Downing and Williams (1975) for the 2.13 µm and

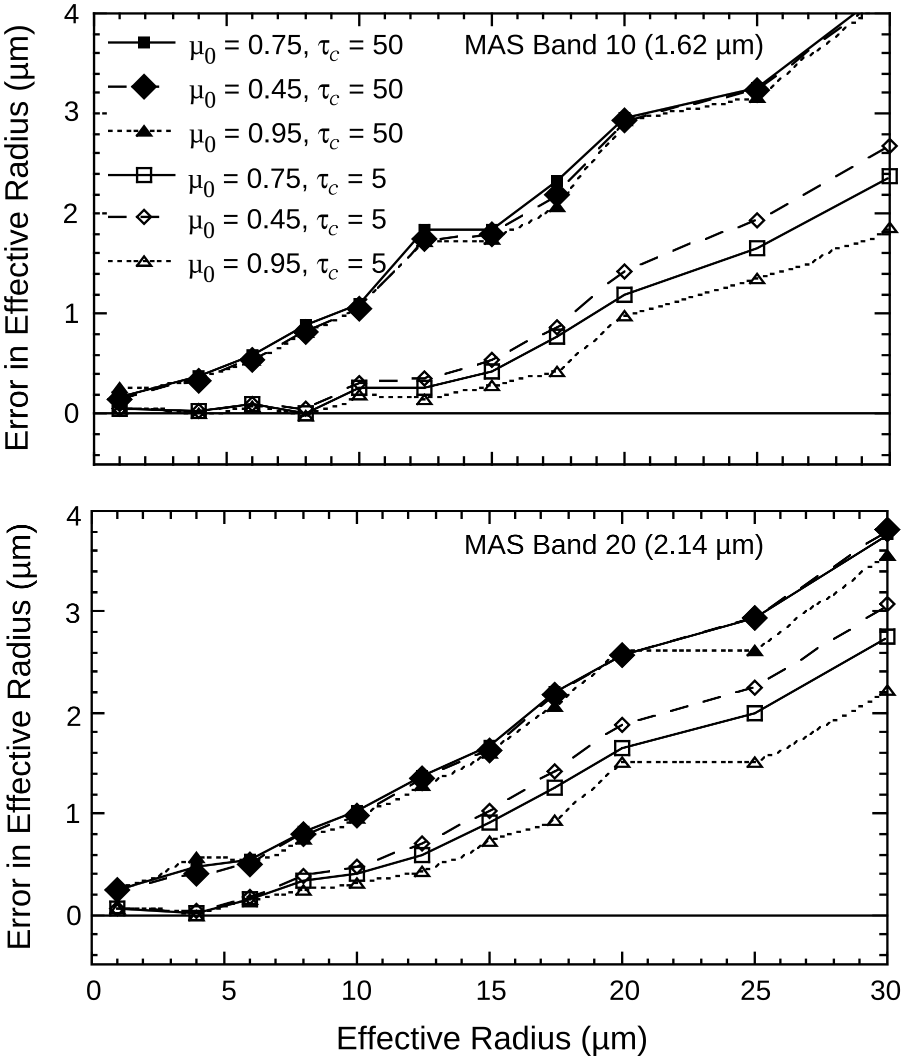

Figure 18. Error in the retrieval of r_e (μm) between using spectrally averaged reflection function calculations based on liquid water optical constants (i) reported by Irvine and Pollack (1968) and (ii) measured by Palmer and Williams (1973). These results were obtained with $\mu = 0.95$ for the MAS 1.62 μm band (top) and the MAS 2.14 μm band (bottom).

greater bands. For visible bands below 0.69 μm, we have used the optical constants tabulated by Hale and Querry (1973).

While this model uncertainty arises from an inadequate knowledge of two physical quantities, those quantities are fixed; it is accurate data that are lacking. The same can be said for the extraterrestrial solar flux needed to calculate the reflection function from calibrated intensity observations.

3.2.2. Physical uncertainties

Physical uncertainties arise due to *changing* physical quantities, such as changes in the above cloud atmosphere (i.e., aerosol loading, thin cirrus, water vapor, molecular scattering) and instrument calibration changes. These examples affect, respectively, the signal received at the satellite and its subsequent value as interpreted by the instrument. Both can be lumped together and ascribed to an overall error in determining the cloud reflection function at wavelength λ_i ($\Delta R^{i}_{\mathrm{meas}}$).

Due to the multiwavelength nature of our cloud retrieval algorithm, together with the near orthogonality of the retrieval of τ_c and r_e (cf. Fig. 9), it is useful to examine the errors in τ_c arising from uncertainties in the visible reflectance, and errors in r_e arising from uncertainties in the near-infrared reflectance. Figure 19 presents an analysis of errors in r_e due to a 1, 2, 5, or 10% error in the reflection function in the near-infrared for MAS ($\Delta R^{2.14}_{\mathrm{meas}}$). Calibration errors are expected to be within 2% for the MODIS 0.65, 1.64 and 2.13 µm bands. Atmospheric transmission to cloud top, direct plus diffuse, is likely to be about 90-95% for most bands, causing a minimum of about a 10% reduction in solar reflected signal if no atmospheric correction is taken into account (round trip transmission $\simeq 0.95^2 \simeq 0.9$). Variability in this transmission, together with atmospheric emission in the 3.75 µm band and the effect of aerosol on atmospheric scattering in the visible band, all serve to complicate this analysis. Considering the near-infrared bands alone, if our ability to account for this variability is limited to 10%, then Fig. 19 suggests that we can only expect that the effective radius can be derived to an uncertainty Δr_e within 1-3 µm for optically thick clouds (depending on the band used). This analysis, summarized in Table 3, is limited to a few solar and observational geometries and optical thicknesses, and thus there is no certainty

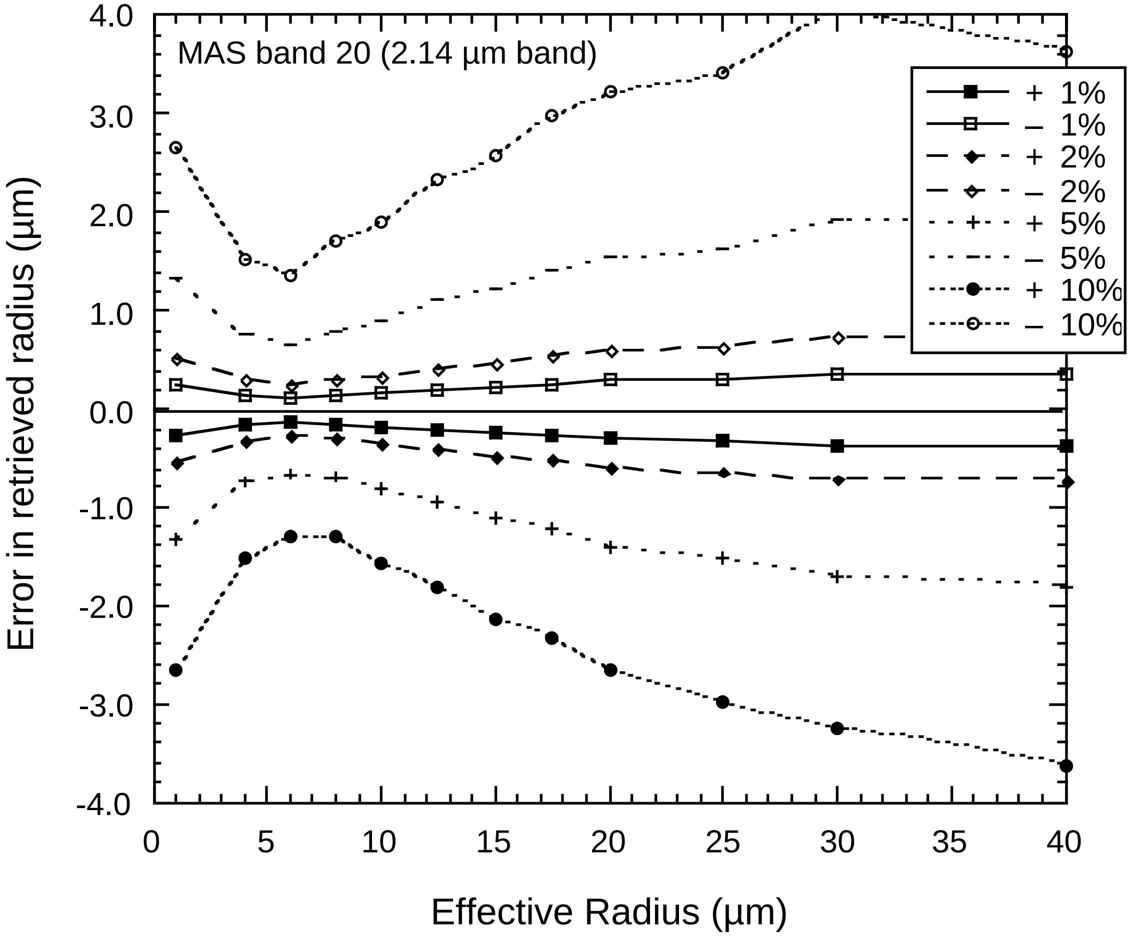

Figure 19. Error in the retrieval of r_e (µm) between (i) using spectrally averaged reflection functions, sensor and solar weighted with 11 wavelengths, and (ii) reflection function measurements assuming an error of ±1, 2, 5, and 10%. These results were obtained using the MAS 2.14 µm band with $\mu_0 = 0.75$, $\mu = 0.95$, $\tau_c = 50$, and the optical constants of Irvine and Pollack (1968).

that errors in excess of these estimates might not sometimes arise.

Determining the effect of atmospheric variability on the retrieval of cloud optical and microphysical properties is an important aspect of ongoing research. Additional sources of model error being investigated include the effects of the size distribution (i.e., effective variance) and in-cloud water vapor absorption.

The previous analysis was for errors in the near-infrared reflection function only. To assess the overall uncertainties in the retrieved optical thickness and effective radius, Nakajima and King (1990) performed radiative transfer computations at 0.75, 1.65 and 2.16 µm. At each wavelength the reflection function was computed for θ_0 = 10, 60°, θ = 0, 10, 30, 50°, ϕ = 0, 10, 30, 60, 120, 150, 170, 180°, τ_c = 4, 8, 16, 32, and r_e = 4, 8, 16 µm.

After confirming that the algorithm returns the correct values of τ_c and r_e for simulated measurements with no observational error, they introduced observational error of 5% into the reflection function at one band, with no observational error in either of the other two bands.

The results of these simulations are presented in Fig. 20, which shows the relationship between errors in r_e and τ_c for 5% error in the reflection function at

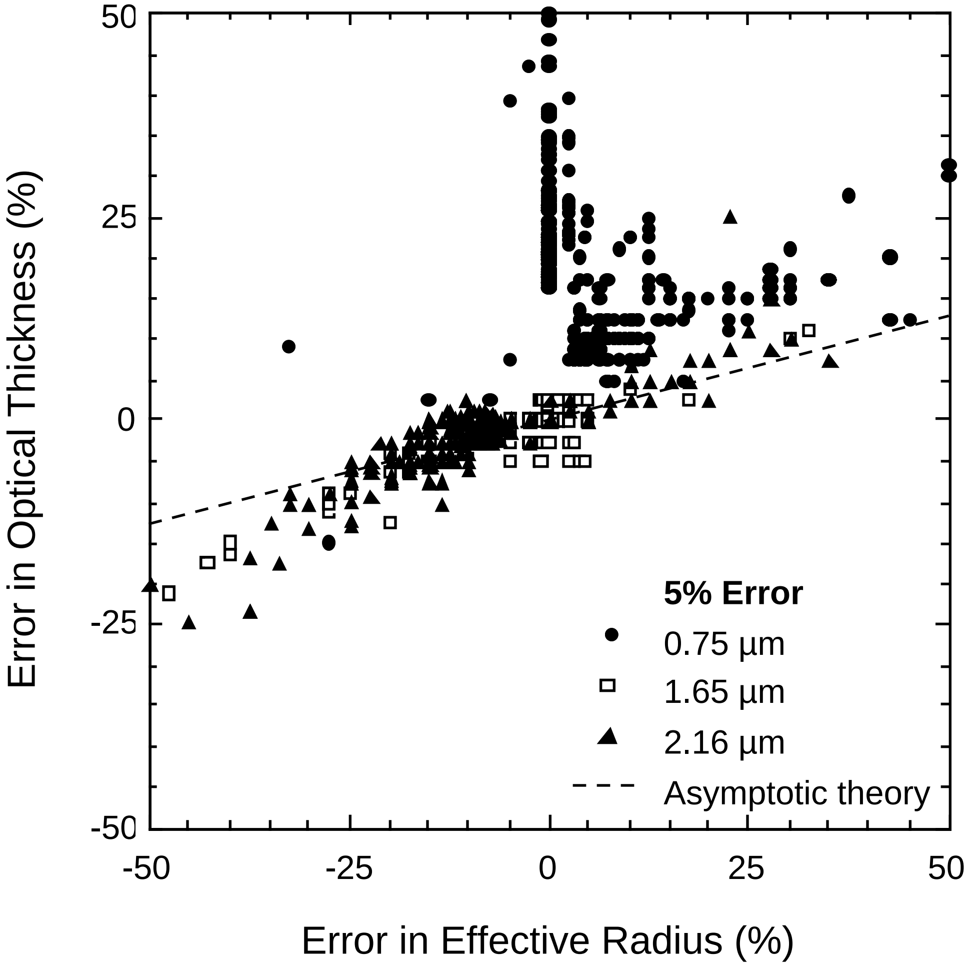

Figure 20. Simultaneous errors in the retrieved optical thickness and effective radius for simulations containing 5% error in the reflection function at 0.75 µm (solid circles), 1.65 µm (open squares), or 2.16 µm (solid triangles). The dashed curve superimposed on these results is the error predicted by Eq. (20) (see text for details) [from Nakajima and King (1990)].

0.75 µm (solid circles), 1.65 µm (open squares) and 2.16 µm (solid triangles). While there are instances for which the error in τ_c is large when the error in r_e is negligible, the overall tendency of these simulations is for an error in τ_c to occur whenever there is an error in r_e. The former condition corresponds to the situation in which the optical thickness is large and measurement (or calibration) errors are confined solely to 0.75 µm. The latter condition, on the other hand, occurs primarily when measurement errors occur at 1.65 or 2.16 µm with no corresponding errors at 0.75 µm. The relationship between errors in τ_c and r_e may be understood as follows. For optically thick layers the reflection function at a nonabsorbing wavelength is primarily a function of the scaled optical thickness, and thus the scaled optical thickness retrieved by our analysis is nearly independent of particle radius. Thus,

$$\frac{\partial \ln \tau_c'}{\partial \ln r_e} = \frac{\partial \ln(1-g)}{\partial \ln r_e} + \frac{\partial \ln \tau_c}{\partial \ln r_e} \simeq 0. \tag{18}$$

From computations of the asymmetry factor as a function of effective radius (Table 4), it follows that at 0.75 µm,

$$\frac{\partial \ln(1-g)}{\partial \ln r_e} \simeq -0.50 + 0.15 \ln r_e. \tag{19}$$

In the radius range $4 \lesssim r_e \lesssim 6$ µm, where the error in effective radius is especially large, a combination of Eqs. (18) and (19) leads to

$$\frac{\partial \ln \tau_c}{\partial \ln r_e} \simeq 0.26. \tag{20}$$

This result, shown in Fig. 20 as a dashed line, is seen to be a reasonable approximation for $|\Delta r_e / r_e| \lesssim 25\%$ and for cases in which the measurement error is confined largely to 1.65 or 2.16 µm. The large errors in droplet radius, which are generally associated with errors in excess of those predicted by Eq. (20), arise primarily when τ_c and r_e are small, cases for which asymptotic theory and the

Table 4. Optical properties of the cloud droplet polydispersions used in the numerical simulations.*

	$\lambda = 0.75$ µm $m = 1.332 - 0.0i$	$\lambda = 2.16$ µm $m = 1.294 - 0.00035i$			$\lambda = 3.70$ µm $m = 1.374 - 0.0036i$		
r_e	g	ω_0	g	k	ω_0	g	k
2.13	0.782	0.99708	0.853	0.0360	0.9783	0.790	0.119
3.00	0.812	0.99578	0.836	0.0458	0.9747	0.802	0.125
4.25	0.832	0.99288	0.803	0.0652	0.9627	0.783	0.160
6.00	0.846	0.98880	0.801	0.0824	0.9387	0.756	0.217
8.50	0.856	0.98408	0.828	0.0917	0.9099	0.775	0.256
12.00	0.862	0.97786	0.850	0.1019	0.8811	0.819	0.275
17.00	0.867	0.96949	0.863	0.1160	0.8465	0.850	0.302
24.00	0.870	0.95849	0.874	0.1321	0.8045	0.872	0.336
34.00	0.873	0.94398	0.885	0.1508	0.7558	0.893	0.375

* All computations were performed assuming a log-normal size distribution with $\sigma = 0.35$ ($v_e = 0.13$).

assumption of Eq. (18) are no longer valid. In a one band method for determining the cloud optical thickness (cf. King 1987, Rossow et al. 1989), where it is necessary to assume a value of r_e, Fig. 20 suggests that errors of ±25% can arise in the optical thickness for errors of ±50% in effective radius.

3.3. *Practical considerations*

3.3.1. *Numerical computation considerations*

a. *Parameter description*

Our group is currently committed to producing three physical parameters as part of MODIS product MOD06 *(Cloud Product*). Two will be ready at-launch and one post-launch. Their dimensions, physical units and storage data types are summarized in Table 5. Parameter 1780 *(Effective Particle Radius)* has units of µm (10^{-4} cm), and ranges from 0 to 100. Parameter 2311 (*Cloud Optical Thickness*) is dimensionless, and ranges from 0 to 100. Parameter 1764 (*Cloud Particle Phase*) is a post-launch parameter having seven states ranging from 0 to 6, corresponding to the following translation: 0–clear, 1–opaque water cloud, 2–opaque ice cloud, 3–mixed phase cloud, 4–non-opaque ice cloud, 5–non-opaque water cloud, and 6–uncertain.

Although reported *Effective Particle Radius* values are retrieved using the 2.13 µm band in conjunction with a non-absorbing visible band, two other methods of retrieval are also performed in our algorithm, viz., a 1.64 and a 3.75 µm band retrieval method, each in conjunction with a corresponding visible band. Results from these two alternate methods are expressed in terms of the *Effective Particle Radius Difference,* which contains the differences in the retrieved effective radius between the 1.64 and 2.13 µm methods, and between the 3.75 and 2.13 µm methods.

The *Cloud Mask 1km* science data set consists of 1 byte per pixel, and contains the first byte from Product MOD35 (*Cloud Mask*). The *Quality Assurance 1km* vector consists of 5 bytes per pixel, and consists of (i) the first byte from Product MOD35 (*Cloud Mask*), (ii) confidence levels of retrieved parameters, such as cloud optical thickness, effective radius, and thermodynamic phase, (iii) retrieval processing path flags, and (iv) input data resource flags. The input data (also referred to as ancillary data) resource QA flags identify the origins of various input data sets, whether from NCEP, DAO or other MODIS products. The retrieval processing path QA flags keeps track of which processing path is taken in the algorithm (either water, ice or mixed phase cloud), what types of atmospheric cor-

Table 5. Summary of MOD06 output parameters produced by Cloud Retrieval Group (based on MOD06 file specification Version 2.0).*

Parameter Name	Dimensions*	Units	Data Type
Effective_Particle_Radius	1354 × 2030	µm	integer*2
Cloud_Optical_Thickness	1354 × 2030	none	integer*2
Cloud_Particle_Phase	1354 × 2030	none	byte
Effective_Particle_Radius_Difference	2 × 1354 × 2030	µm	integer*2
Cloud_Mask_1km	1354 × 2030	none	byte
Quality_Assurance_1km	5 × 1354 × 2030	none	byte
Statistics	20		real*2

* Nominally, a 1 km resolution MODIS granule has 1354 pixels cross track and 2030 detector lines along track (5 min).

rection are used (Rayleigh and/or water vapor), and what band is used for the optical thickness retrieval. The confidence level QA of a retrieved parameter (e.g., cloud optical thickness), is three bits long (per pixel): 1 bit is a useful-or-not useful indicator, immediately followed by 2 bits of confidence levels (0 - 3). The most updated and complete description of the quality assurance flags can be found in a separate document (Chu et al. 1997).

Finally, the *Statistics* array consists of 20 bytes representing statistics computed over the entire MODIS granule. The first 15 values are computed as follows:

1. Successful retrieval rate;
2. Land cover fraction;
3. Water cover fraction;
4. Snow cover fraction;
5. Cloud cover fraction;
6. Water cloud detected;
7. Ice cloud detected;
8. Mean of water cloud optical thickness;
9. Standard deviation of water cloud optical thickness;
10. Mean of ice cloud optical thickness;
11. Standard deviation of ice cloud optical thickness;
12. Mean of water cloud effective particle radius;
13. Standard deviation of water cloud effective particle radius;
14. Mean of ice cloud effective diameter;
15. Standard deviation of ice cloud effective diameter.

The remaining 5 bytes are currently undefined and are therefore available as spares for future enhancements.

b. Required input data

The MODIS Level-1B calibrated radiance (MOD02) and geolocation fields (MOD03) are needed by all three retrieved parameters, *Cloud Optical Thickness*, *Effective Particle Radius*, and *Cloud Particle Phase.* Processed by MCST, the MOD02 product is archived in three separate files, one of which (MOD02_1km) provides all 36 MODIS bands at effective 1 km spatial resolution, based on integrating the 250 and 500 m pixels according to an approximate point spread function of the MODIS instrument.

In retrieving the *Cloud Optical Thickness* and *Effective Particle Radius,* seven additional inputs, or ancillary data sets, are required (cf. Table 6). NCEP gridded analysis and other MODIS data products can be ingested into our retrieval program in real-time, whereas DAO data are only available for re-analysis (>72 hours after data acquisition). Except MOD35 (*Cloud Mask*), all other ancillary data sets are first handled by ancillary data subroutines and then made available

TABLE 6. Ancillary data sets needed by cloud optical thickness and effective particle radius retrieval (MOD_PR06OD).

Ancillary Data Categories	Data Sources
Cloud Top Pressure and Temperature	MOD06 DAO
Cloud Mask	MOD35
Land Surface Temperature	NCEP DAO MOD11
Sea Surface Temperature	NCEP DAO MOD28
Atmosphere Temperature Profile	NCEP DAO MOD07
Atmosphere Moisture Profile	NCEP DAO MOD07
Surface Spectral Albedo	MOD43 CERES / SARB

to the main retrieval program at every pixel that is identified as containing cloud. In cases where there are multiple data sources, only one is chosen, depending on the availability of the data source at the time of processing and based on production rules set by the Cloud Retrieval Group.

In the post-launch period, the MODIS aerosol product MOD04 will also be useful for studying aerosol-cloud interactions and their effects on cloud retrievals.

c. Data processing path and requirements

The retrieval algorithm outlined in section 3.1 is implemented in practice as follows:

- set ECS core metadata which contains information about a MODIS product that is used for catalog, search, and archival purposes;
- read *Cloud Mask* information to determine if a given pixel is cloudy or clear, and determine whether it is a water, ice, or mixed phase cloud;
- call ancillary data subroutines to gather ancillary input data sets;
- read Level-1B data (MOD02_1km) and geolocation fields (MOD03_L1A): one instrument scan (10 detector lines) of MODIS data at a time for seven spectral bands (0.645, 0.858, 1.240, 1.640, 2.13, 3.75 and 11.03 µm). Information about the viewing geometry (μ, μ_0 and ϕ) is also obtained at this stage;
- apply atmospheric corrections (Rayleigh, water vapor and other absorbing gases) to the radiance data;
- perform cloud property retrieval, using either ice or water table look-up libraries, depending on the thermodynamic phase (cf. Figure 12);
- output results to MOD06 data product.

The efficient processing speed of the cloud retrieval code has been improved by about a factor of 4 since the ß version of the code was first delivered. With the delivered version 1 code, the MODIS Science Data Support Team (SDST) estimated that it requires about 375 MFLOPS to generate parameters 1780 (*Cloud Effective Particle Radius*) and 2311 (*Cloud Optical Thickness*) with confidence level values for daily observations over the entire globe (day time only). This includes a factor of 1.6 for additional time needed for data production, a factor of 0.4 for cloudy scenes, and a factor of 2 for atmospheric corrections. The version 2 (at-launch) code has now been developed, and it includes metadata, QA, atmospheric correction, and ancillary files, and hence these scale factors are no longer required. At the moment, no timing estimates have yet been made for a sufficient number of granules to see what the level-2 sustained (orbital average) processing rate is expected to be at-launch.

Parameter 1764 (*Cloud Particle Phase*) is a post-launch parameter. The required data processing speed is not available at this time, since no prototype code has yet been developed. However, we estimate that, based on some of our research code, about 20 MFLOPS should be sufficient.

d. Data storage estimates

The following storage estimates are based on the file specification (Version 2.0) for elements of the MOD06 product produced by the cloud optical depth process (MOD_PR06OD). This storage is separate and distinct from the storage requirements of the Menzel and Strabala cloud top properties process (MOD_PR06CT) and the Gao cirrus detection process (MOD_PR06CD). At 1 km spatial resolution, the MODIS Science Data Support Team (SDST) estimates 4×10^8 pixels per day over sun-lit portions of the Earth (2.7 million pixels per granule multiplied by 144 granules per day). The Cloud Retrieval Group produces day-time only parameters, and the storage requirements for all of these elements amounts to ~6 GB per day (see below).

Parameter 1764 (*Cloud Particle Phase*) has values ranging from 0 to 6 and can be stored as a single byte per pixel. This parameter will be derived for each 1 km cloudy pixel during the daytime. Thus the data storage required per day, separate from the Menzel and Strabala (1997) infrared cloud particle phase algorithm, is approximately

$$(4 \times 10^8 \text{ pixels}) \times 1 \text{ byte/pixel} = 400 \text{ Mbytes.}$$

Parameters 1780 *(Effective Particle Radius)* and 2311 (*Cloud Optical Thickness)* have values ranging from 0 to 1000. These parameters are both scaled by a factor of 10 and stored as 16 bit integers, and are derived for each cloudy 1 km pixel over the entire globe once per day (day time only). Thus the data storage required per day is approximately

$$(4 \times 10^8 \text{ pixels}) \times 2 \text{ bytes/pixel} = 800 \text{ Mbytes}$$

for each of these parameters.

The *Effective Particle Radius Difference* parameter is also scaled up by a factor of 10 and stored as 16 bit integers. Since there are two of these difference for each pixel, the storage requirement for this parameter is

$$2 \times (4 \times 10^8 \text{ pixels}) \times 2 \text{ bytes/pixel} = 1600 \text{ Mbytes.}$$

The *Cloud Mask 1km* parameter consists of 1 byte per pixel, and hence its storage requirement is

$$(4 \times 10^8 \text{ pixels}) \times 1 \text{ byte/pixel} = 400 \text{ Mbytes.}$$

The *Quality Assurance 1km* parameter requires the largest storage space among the six output parameters we produce. It consists of 5 bytes per pixel, and hence its storage requirement is

$$5 \times (4 \times 10^8 \text{ pixels}) \times 1 \text{ byte / pixel} = 2000 \text{ Mbytes.}$$

Thus the total storage required for all MOD_PR06OD parameters per day is approximately

$$(400 + 800 + 800 + 1600 + 400 + 2000) \text{ Mbytes} = 6.0 \text{ Gbytes,}$$

of which the 400 Mbyte *Cloud Particle Phase* requirement is only required post-launch. As a consequence, this parameter is not currently included in the at-launch file spec, resulting in the at-launch requirement of ~5.6 Gbytes / day.

This estimated figure can easily be reduced by carefully selecting the smallest data type while still satisfying the precision requirement. The *Effective Particle Radius Difference* is currently scaled and stored as 16 bit integers. By definition, this parameter is the differences in the retrieved effective radius between the 1.64 and 2.13 µm methods, and between the 3.75 and 2.13 µm methods. Presumably the differences are quite small. A byte data type, rather than a short integer, might be sufficient. This would result, if implemented, in an 800 Mbyte savings in storage space per day.

The storage space requirement can be further reduced if a compression algorithm is used. As stated above, all MOD06 data parameters are produced only over cloudy pixels, and the cloud-free regions are filled with missing values. Standard compression algorithms work well for this type of data set. HDF release version 4.1 supports all standard HDF compression algorithms:[4] JPEG, Adaptive Huffman, GZIP “deflation,” (Lempel / Ziv-77 dictionary coder), and Run-length encoding. In the future, Lempel / Ziv-78 dictionary coding, an arithmetic coder, and a faster Huffman algorithm may be included. See the *HDF 4.1 User’s Guide* for more information.

---

[4] The *Sdsetcompress* routine is only available in C interface at the time of writing.

e. Level-3 gridded cloud data

The Level-3 Atmosphere Joint Product (MOD08) algorithm combines parameters from multiple MODIS atmosphere products including aerosols, cloud properties, precipitable water, and atmospheric profiles. The integrated atmosphere product will be produced on a daily, 8-day and monthly time scale, each of which will be produced at both an equal angle (1° × 1°) and equal area (~100 km) spatial scale (cf. Fig. 1). Daily and monthly equal angle grids will be prepared at launch, with the other products to follow. We will compute statistics separately for pixels identified as water and ice clouds. Statistics will include the parameters of normal and log-normal distributions in two ways (including and excluding the effects of our Quality Assurance estimates) and the fraction of ice-cloud and water-cloud pixels in each grid box. We will also provide histograms of optical thickness and effective particle size, and joint histograms of both optical thickness and effective particle size with both cloud top temperature and cloud effective emissivity (the latter two quantities coming from Menzel and Strabala's algorithm). After launch we anticipate computing statistics for liquid and ice water path, derived as $W = 2\rho\tau_c r_e / 3$, where ρ is the density of water.

We have not yet determined the best way to categorize the various quality control indicators into our joint level-3 product, in part because we lack a complete theoretical understanding of the magnitudes of errors we expect in varying circumstances. Such assessments, however, will be very important to our ability to diagnose global indicators of algorithm strengths and weaknesses. Steve Platnick was recently chosen as Principal Investigator under a funding announcement for the EOS Calibration and Validation program, and we anticipate making substantial use of his results to determine the QA for our Level 2 and Level 3 products. We will produce a separate ATBD that describes the joint level-3 atmosphere algorithm for MODIS.

3.3.2. Validation

Products from the present algorithm have been tested using MCR data (Nakajima et al. 1991) as well as from ongoing research projects that utilize MAS data, as described in Section 2.2. Several field programs offer opportunities for pre-launch and post-launch MODIS validation through collection and analysis of observations obtained from the MODIS Airborne Simulator (MAS; King et al. 1996) and High-spectral resolution Interferometer Sounder (HIS; Smith et al. 1995). These field campaigns, principal focus, and MODIS atmosphere group participants, are summarized in Table 7.

TABLE 7. Research & Analysis, and post-launch specific airborne validation campaigns planned by the MODIS atmosphere group within 3 years of launch of AM-1. This table includes the primary purpose of the mission as well as the responsible team members and key associates.

Mission	*Dates*	*Responsible Team Members*	*Primary Purpose*
FIRE III	May-June 1998	Michael King, Si-Chee Tsay, Steve Platnick, Steve Ackerman	arctic stratus clouds over sea ice
MODIS-specific validation campaigns			
ARM-2	March 1999	Michael King, Si-Chee Tsay, Steve Platnick, Steve Ackerman	periodic flights over the NSA ARM site with MAS & HIS
California	July 1999 December 1999	Michael King, Steve Platnick, Si-Chee Tsay	marine stratocumulus (July) and valley fog (December)
Kalahari Desert	August-September 1999	Michael King, Yoram Kaufman, Si-Chee Tsay, Steve Platnick, Didier Tanré, Lorraine Remer	smoke, clouds and radiation from biomass burning in the Savannah; marine stratocumulus off Namibian desert; surface BRDF

In addition to these ER-2 field campaigns, which often include the Cloud Lidar System (CLS; Spinhirne et al. 1989) for verifying cloud top altitude and multi-layer clouds, the University of Washington CV-580, with the Cloud Absorption Radiometer (CAR; King et al. 1986) and extensive in situ cloud microphysics (liquid water content, effective radius, cloud drop size distribution), aerosol properties (size distribution, scattering and absorption coefficients), and meteorological sensors, will be used as required.

In addition to these airborne campaigns in which we directly intend to participate, we expect to make use of selected ground-based networks (cf. Table 8).

The ground-based measurements will be obtained on a continuous basis as well as during intensive field experiments. All of these validation opportunities, as well as intercomparison of data derived from MODIS with other sensors on AM-1 and other spacecraft, will be discussed in detail below.

Validation will be approached in several ways: (i) collocation with higher resolution aircraft data, (ii) ground-based and aircraft in situ observations, and (iii) intercomparisons with other AM-1 instruments. Our validation approach relies heavily on the sources of the data that were used in the algorithm devel-

TABLE 8. Surface networks that the MODIS atmosphere group plans to utilize, including the primary purpose of the network and the responsible team members and key associates.

Network	*Location*	*Responsible Team Members*	*Primary Purpose*
AERONET	multiple locations: US, Japan, South America, Africa, & Europe	Brent Holben, Yoram Kaufman, Didier Tanré	aerosol optical thickness and columnar size distribution
ARM	Oklahoma, North Slope of Alaska, Western Tropical Pacific	Paul Menzel, Si-Chee Tsay	cloud base height (micropulse lidar), temperature and moisture profiles, sky radiance (visible and IR)

opment, which consisted primarily of the MAS, HIS, and AVIRIS, a 224 band imaging spectrometer from 0.4-2.5 µm with 20 m resolution at nadir (Vane et al. 1993).

Since the spatial resolution of the MAS data is much smaller than that of MODIS, we plan to use various types of spatial resolution data, such as degraded MAS data, to test the algorithm during the pre-launch stage. In particular, we will use the recently upgraded MAS 50 band 12 bit data, together with cloud mask information from Ackerman et al.'s (1997) algorithm, to test our cloud retrieval algorithm.

In the first two years following the launch of EOS AM-1, we anticipate collecting the following data sets for the purpose of validating MODIS algorithms and data products through direct intercomparisons of MODIS data with in situ and airborne remote sensing data sets. These campaigns will be EOS-targeted campaigns of direct relevance to assuring the accuracy of MODIS-derived data products, and are summarized in Table 9.

The first EOS-targeted campaign after the MODIS launch will be coordinated with measurements taken at the North Slope Alaska (NSA) ARM site in Barrow, Alaska, probably in March 1999. The ER-2 with MAS, Scanning HIS, CLS, Air-MISR, and RAMS will be deployed to synchronize with the MODIS overflight; the ARM site suite of ground-based measurements (class-sonde, AERI, tower measurements of temperature and moisture at various elevations, microwave moisture measurements, lidar and radar observations, whole sky imagers) will be collected simultaneously. These combined air and ground measurements will be used to validate MODIS radiance measurements. Results will be used to adjust the infrared calibration coefficients as necessary. In addition, the ARM ground-based measurements can be used to validate geophysical parameters as

TABLE 9. EOS-targeted airborne field campaigns planned by the MODIS atmosphere group within 3 years after the launch of AM-1. This table includes the primary purpose of the campaign as well as the principal sensors to be used, responsible team members and key associates, and primary purpose.

EOS-Targeted Field Campaign	*Principal Sensors*	*Responsible Team Members*	*Primary Purpose*
ARM overflights (SGP & NSA)	MAS, HIS, CLS, AERI, surface lidar & microwave sensors	Steve Ackerman, Paul Menzel, Bo-Cai Gao, Si-Chee Tsay	mid-latitude cirrus clouds over continents, Arctic stratus over sea ice and tundra
California	MAS, CLS, AirMISR	Michael King, Steve Platnick, Si-Chee Tsay	marine stratocumulus and valley fog
Kalahari Desert	MAS, AirMISR, CLS, CAR, in situ microphysics, AERONET	Michael King, Yoram Kaufman, Si-Chee Tsay, Steve Platnick, Didier Tanré, Lorraine Remer	smoke, clouds and radiation from biomass burning in the Savannah; marine stratocumulus off Namibian desert; surface BRDF

well. Lidar and radar observations of cloud boundaries over the ARM sites will be used to validate the presence of a cloud as well as its cloud top pressure altitude. Whole sky imagers are also available at the site, and can be used to compare satellite and ground-based estimates of cloud amount. Finally, optical depth measurements derived from lidar will aid in specifying the limit of thin cirrus detection in the cloud mask algorithm.

Once the MODIS is in orbit and returning regular data, we envision two focused periods of ER-2 overflights, to be coordinated with the EOS AM-1 orbit, in California (the first one over marine stratocumulus clouds located over the ocean between Monterey and San Diego in July 1999, and the second over valley fog in the central valley of California in December 1999). These experiments would entail ER-2 flights from home base in California (Dryden Flight Research Center), and would consist, once again, of the MAS and CLS, together with coordinated underflights by the University of Washington CV-580 with its in situ microphysics probes. This data set, of special interest to Goddard Space Flight Center (Michael King, Steve Platnick, Si-Chee Tsay), would help to validate the cloud optical thickness and effective radius between MODIS and the smaller spatial resolution airborne sensors on the ER-2.

In collaboration with the MODIS Land Group as well as MISR, CERES, MOPITT, and ASTER, we plan to conduct a 4 week experiment on biomass burning in the Savannah region of southern Africa (near the Kalahari Desert of Namibia). Biomass burning occurs in August-September, as in South America, so we plan to conduct this experiment in August-September 1999, well after the launch of AM-1. Opportunities to study Namibian marine stratus or other cloud types may also be available. This experiment, like SCAR-B in 1995, will entail both the NASA ER-2 aircraft as well as the University of Washington CV-580. Primary instruments of interest for the ER-2 are the MAS, scanning HIS, CLS, AirMISR, SSFR, and RAMS. The latter two instruments are to characterize spectral and broadband flux of particular relevance to CERES objectives. As in Brazil (SCAR-B), we will coordinate the ER-2 with in situ aerosol and chemistry measurements on the CV-580 and overfly numerous AERONET locations in Namibia, South Africa, Zambia, and Zimbabwe.

Additional post-launch EOS-targeted field campaigns are discussed in the MODIS Atmospheres Validation Plan (http://eospso.gsfc.nasa.gov/validation/valplans.html). During the post-launch stage, it is anticipated that one full day of MODIS data at the 1 km pixel resolution per month will be sufficient for algorithm testing and validation purposes. We only require the spectral bands used in our algorithm, but would also be interested in selected thermal bands to test the performance of the cloud mask algorithm. When a major algorithm revision is made, we will require a large data set to test and validate the algorithm. Eight days of MODIS level-1B data (for the bands given in Table 1) every month will be sufficient for this purpose.

Algorithm changes will be restrained to occur once per year as needed. We anticipate assessing the performance of the MODIS algorithms initially by processing 8 contiguous days per month, as well as specific time periods with validation experiments of special relevance, as outlined above. After initially looking at one year's data, consistency checks, quality assurance flags, validation campaigns, as appropriate, and intercomparisons with other instruments (especially on AM-1), we will begin whole-scale reprocessing, including every month. This initial stage may take in excess of one year, during which time the MODIS calibration algorithm will likely undergo additional refinement. Continual refinement of the MODIS "operational" algorithms will largely be conducted at the Team Member's SCF as well as at the Team Leader Computing Facility (TLCF), as many of the algorithms are dependent on results from other algorithms (like calibration). Only periodically (after say 1.5 years following launch), the first reprocessing at the DAAC will be initiated.

This validation plan represents the thought process of all MODIS atmosphere team members, associates, and close colleagues. This group has considerable field campaign experience as well as experience with other satellite and surface network data. Putting all MODIS validation schedules together that relate to the cloud optical thickness, effective radius, and thermodynamic phase algorithms described in this ATBD, we obtain the "master schedule" for MODIS cloud validation activities, for the focused, field-campaign portion of this plan (cf. Figure 21).

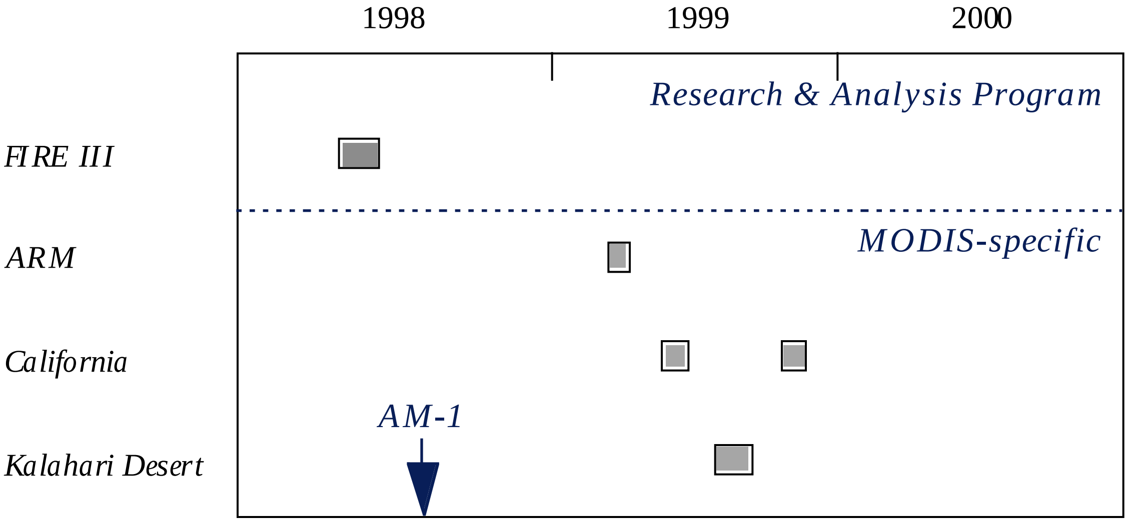

Figure. 21. ER-2 Validation strategy for the MODIS cloud optical thickness, effective radius, and thermodynamic phase algorithms from 1998 (pre-launch) through 2000 (post-launch).

3.3.3. *Quality control, diagnostics, and exception handling*

The quality control and diagnostics of all post-launch products will be performed based on comparisons with field programs in which related *in situ* cloud microphysical data are available. This type of exercise may provide some insights into refining the algorithm. Special cases of missing data, extremely low sun angles, and the presence of sun glint will be handled separately.

4. *Constraints, limitations, and assumptions*

There are several assumptions involved in the theoretical development of cloud particle size and optical thickness retrievals. At the present time, the algorithm is valid for single-layer, liquid water, plane-parallel geometry. Cloudy pixels that encounter multiple-layer and horizontal inhomogeneity will not be retrieved correctly. Further developments in the area of detecting multilayer cloud systems and of correcting for geometrical effects are needed. Also, some errors are expected to be encountered in retrieved cloud effective particle radius and optical thickness when ice clouds are present. We currently envision a switch (outlined above) for processing data using a Mie theory phase function for water clouds and an ice crystal phase function derived for hexagonal crystals for ice clouds (cf. Fig. 8). Finally, we have yet to determine the upper limit to the solar zenith angle for which our algorithm can reliably be applied. Unsatisfactory results will no doubt occur when the solar zenith angle $\theta_0 \gtrsim 80°$, a switch that must be set in the operational code. In addition to reduced sensitivity for large solar zenith angles, there are additional complications arising from increased probability of shadows and finite and 3-dimensional cloud effects. This is a problem that exists with all such solar cloud reflectance algorithms, and we currently plan to set this $\theta_0^{\max} = 80°$.

5. References

Ackerman, S., K. Strabala, P. Menzel, R. Frey, C. Moeller, L. Gumley, B. Baum, C. Schaaf, and G. Riggs, 1997: *Discriminating Clear-Sky from Cloud with MODIS: Algorithm Theoretical Basis Document (MOD35)*. Algorithm Theoretical Basis Document ATBD-MOD-06, NASA Goddard Space Flight Center, 125 pp.

Arking, A., 1964: Latitudinal distribution of cloud cover from TIROS III photographs. *Science*, **143**, 569–572.

_____, and J. D. Childs, 1985: Retrieval of cloud cover parameters from multispectral satellite images. *J. Climate Appl. Meteor.*, **24**, 322–333.

Bevington, P. R., 1969: *Data Reduction and Error Analysis for the Physical Sciences.* McGraw-Hill, 336 pp.

Cess, R, D., G. L. Potter, J. P. Blanchet, G. J. Boer, S. J. Ghan, J. T. Kiehl, H. Le Treut, Z. X. Li, X. Z. Liang, J. F. B. Mitchell, J. J. Morcrette, D. A. Randall, M. R. Riches, E. Roeckner, U. Schlese, A. Slingo, K. E. Taylor, W. M. Washington, R. T. Wetherald and I. Yagai, 1989: Interpretation of cloud-climate feedback as produced by 14 atmospheric general circulation models. *Science*, **245**, 513–516.

Chu, A., K. Strabala, R. Song, S. Platnick, M. Wang and S. Mattoo, 1997: *MODIS Atmosphere QA Plan*, NASA Goddard Space Flight Center, 43 pp.

Cline, A. K., 1974: Scalar- and planar-valued curve fitting using splines under tension. *Comm. Assoc. Comput. Mach.*, **17**, 218–220.

Curran, R. J., H. L. Kyle, L. R. Blaine, J. Smith and T. D. Clem, 1981: Multichannel scanning radiometer for remote sensing cloud physical parameters. *Rev. Sci. Instrum.*, **52**, 1546–1555.

_____, and M. L. C. Wu, 1982: Skylab near-infrared observations of clouds indicating supercooled liquid water droplets. *J. Atmos. Sci.*, **39**, 635–647.

DAO, 1996: *Algorithm Theoretical Basis Document for Goddard Earth Observing System Data Assimilation System (GEOS DAS) with a focus on Version 2*. ATBD-DAO-01, NASA Goddard Space Flight Center, 131 pp.

Downing, H. D., and D. Williams, 1975: Optical constants of water in the infrared. *J. Geophys. Res.*, **80**, 1656–1661.

Durkee, P. A., 1989: Observations of aerosol-cloud interactions in satellite-detected visible and near-infrared radiance. *Proc. Symposium on the Role of Clouds in Atmospheric Chemistry and Global Climate*, American Meteorological Society, Anaheim, CA, 157–160.

Foot, J. S., 1988: Some observations of the optical properties of clouds. I: Stratocumulus. *Quart. J. Roy. Meteor. Soc.*, **114**, 129–144.

Grainger, R. G., 1990: The calculation of cloud parameters from AVHRR data. *Ph.D. Dissertation*, University of Auckland, New Zealand, 188 pp.

Hale, G. M., and M. R. Querry, 1973: Optical constants of water in the 200-nm to 200-µm wavelength region. *Appl. Opt.*, **12**, 555–563.

Han, Q., W. B. Rossow and A. A. Lacis, 1994: Near-global survey of effective droplet radius in liquid water clouds using ISCCP data. *J. Climate*, **7**, 465–497.

_____, W. Rossow, R. Welch, A. White and J. Chou, 1995: Validation of satellite retrievals of cloud microphysics and liquid water path using observations from FIRE. *J. Atmos. Sci.*, **52**, 4183–4195.

Hansen, J. E., and J. B. Pollack, 1970: Near-infrared light scattering by terrestrial clouds. *J. Atmos. Sci.*, **27**, 265–281.

_____, and L. D. Travis, 1974: Light scattering in planetary atmospheres. *Space Sci. Rev.*, **16**, 527–610.

Irvine, W., M., and J. B. Pollack, 1968: Infrared optical properties of water and ice spheres. *Icarus*, **8**, 324–360.

Kaufman, Y. J., and T. Nakajima, 1993: Effect of Amazon smoke on cloud microphysics and albedo. *J. Appl. Meteor.*, **32**, 729–744.

King, M. D., 1981: A method for determining the single scattering albedo of clouds through observation of the internal scattered radiation field. *J. Atmos. Sci.*, **38**, 2031–204.

_____, 1987: Determination of the scaled optical thickness of clouds from reflected solar radiation measurements. *J. Atmos. Sci.*, **44**, 1734–1751.

_____, L. F. Radke and P. V. Hobbs, 1990: Determination of the spectral absorption of solar radiation by marine stratocumulus clouds from airborne measurements within clouds. *J. Atmos. Sci.*, **47**, 894–907.

_____, Y. J. Kaufman, W. P. Menzel and D. Tanré, 1992: Remote sensing of cloud, aerosol and water vapor properties from the Moderate Resolution Imaging Spectrometer (MODIS). *IEEE Trans. Geosci. Remote Sens.*, **30**, 2–27.

_____, M. G. Strange, P. Leone and L. R. Blaine, 1986: Multiwavelength scanning radiometer for airborne measurements of scattered radiation within clouds. *J. Atmos. Oceanic Technol.*, **3**, 513–522.

_____, W. P. Menzel, P. S. Grant, J. S. Myers, G. T. Arnold, S. E. Platnick, L. E. Gumley, S. C. Tsay, C. C. Moeller, M. Fitzgerald, K. S. Brown and F. G. Osterwisch, 1996: Airborne scanning spectrometer for remote sensing of cloud, aerosol, water vapor and surface properties. *J. Atmos. Oceanic Technol.*, **13**, 777–794.

Kou, L, D. Labrie and P. Chylek, 1993: Refractive indices of water and ice in the 0.65- to 2.5-µm spectral range. *Appl. Opt.*, **32**, 3531–3540.

Kratz, D. P., 1995: The correlated k-distribution technique as applied to the AVHRR channels. *J. Quant. Spectrosc. Radiat. Transfer*, **53**, 501–517.

Menzel, W. P., and L. E. Gumley, 1996: *MODIS Atmospheric Profile Retrieval Algorithm Theoretical Basis Document*. ATBD-MOD-07, NASA Goddard Space Flight Center, 32 pp.

_____, and K. Strabala, 1997: *Cloud Top Properties and Cloud Phase: Algorithm Theoretical Basis Document*. ATBD-MOD-04, NASA Goddard Space Flight Center, 55 pp.

Mitchell, J. F. B., C. A. Senior and W. J. Ingram, 1989: CO_2 and climate: A missing feedback? *Nature*, **341**, 132–134.

Nakajima, T., and M. Tanaka, 1986: Matrix formulations for the transfer of solar radiation in a plane-parallel scattering atmosphere. *J. Quant. Spectrosc. Radiat. Transfer*, **35**, 13–21.

_____, and M. D. King, 1990: Determination of the optical thickness and effective particle radius of clouds from reflected solar radiation measurements. Part I: Theory. *J. Atmos. Sci.*, **47**, 1878–1893.

_____, and _____, 1992: Asymptotic theory for optically thick layers: Application to the discrete ordinates method. *Appl. Opt.*, **31**, 7669–7683.

_____, _____, J. D. Spinhirne and L. F. Radke, 1991: Determination of the optical thickness and effective particle radius of clouds from reflected solar radiation measurements. Part II: Marine stratocumulus observations. *J. Atmos. Sci.*, **48**, 728–750.

Nakajima, T. Y., and T. Nakajima, 1995: Wide-area determination of cloud microphysical properties from NOAA AVHRR measurements for FIRE and ASTEX regions. *J. Atmos. Sci.*, **52**, 4043–4059.

Ou, S. C., K. N. Liou, W. M. Gooch, and Y. Takano, 1993: Remote sensing of cirrus cloud parameters using Advanced Very High Resolution Radiometer 3.7 and 10.9 µm channels. *Appl. Opt.*, **32**, 2171–2180.

Palmer, K. F., and D. Williams, 1974: Optical properties of water in the near infrared. *J. Opt. Soc. Amer.*, **64**, 1107–1110.

Pilewskie, P., and S. Twomey, 1987: Cloud phase discrimination by reflectance measurements near 1.6 and 2.2 µm. *J. Atmos. Sci.*, **44**, 3419–3420.

Platnick, S., 1991: Remote sensing the susceptibility of cloud albedo to changes in drop concentration. *Ph.D. Dissertation*, University of Arizona, Tucson, Arizona, 266 pp.

_____, 1997: The scales of photon transport in cloud remote sensing problems. *IRS 96: Current Problems in Atmospheric Radiation*, W. L. Smith and K. Stamnes, Eds., A. Deepak Publishing, 206–209.

_____, and S. Twomey, 1994: Determining the susceptibility of cloud albedo to changes in droplet concentration with the Advanced Very High Resolution Radiometer. *J. Appl. Meteor.*, **33**, 334–347.

_____, and F. P. J. Valero, 1995: A validation study of a satellite cloud retrieval during ASTEX. *J. Atmos. Sci.*, **52,** 2985–3001.

Ramanathan, V., 1987: The role of Earth radiation budget studies in climate and general circulation research. *J. Geophys. Res.*, **92**, 4075–4095.

_____, E. J. Pitcher, R. C. Malone and M. L. Blackmon, 1983: The response of a spectral general circulation model to refinements in radiative processes. *J. Atmos. Sci.* **40**, 605–630.

_____, R. D. Cess, E. F. Harrison, P. Minnis, B. R. Barkstrom, E. Ahmad and D. Hartmann, 1989: Cloud-radiative forcing and climate: Results from the Earth Radiation Budget Experiment. *Science*, **243**, 57–63.

Rawlins, F., and J. S. Foot, 1990: Remotely sensed measurements of stratocumulus properties during FIRE using the C130 aircraft multichannel radiometer. *J. Atmos. Sci.*, **47**, 2488–2503.

Robertson, C. W., and D. Williams, 1971: Lambert absorption coefficients of water in the infrared. *J. Opt. Soc. Amer.*, **61**, 1316–1320.

Roeckner, E., U. Schlese, J. Biercamp and P. Loewe, 1987: Cloud optical depth feedbacks and climate modelling. *Nature*, **329**, 138–140.

Rossow, W. B., F. Mosher, E. Kinsella, A. Arking, M. Despois, E. Harrison, P. Minnis, E. Ruprecht, G. Sèze, C. Simmer and E. Smith, 1985: ISCCP cloud algorithm intercomparison. *J. Appl. Meteor.*, **24**, 877–903.

_____, L. C. Gardner and A. A. Lacis, 1989: Global seasonal cloud variations from satellite radiance measurements. Part I: Sensitivity of analysis. *J. Climate*, **2**, 419–458.

Slingo, A., 1989: A GCM parameterization for the shortwave radiative properties of water clouds. *J. Atmos. Sci.*, **46**, 1419–1427.

Smith, W. L., H. E. Revercomb, R. O. Knuteson, F. A. Best, R. Dedecker, H. B. Howell and H. M. Woolf, 1995: Cirrus cloud properties derived from the high spectral resolution infrared spectrometry during FIRE II. Part I: The

High Resolution Interferometer Sounder (HIS) system.. *J. Atmos. Sci.*, **52**, 4238–4245.

Spinhirne, J. D., R. Boers and W. D. Hart, 1989: Cloud top liquid water from lidar observations of marine stratocumulus. *J. Appl. Meteor*., **28**, 81–90.

Stamnes, K., S. C. Tsay, W. Wiscombe and K. Jayaweera, 1988: Numerically stable algorithm for discrete-ordinate-method radiative transfer in multiple scattering and emitting layered media. *Appl. Opt.*, **27**, 2502–2509.

Stowe, L. L., H. Y. M. Yeh, , T. F. Eck, C. G. Wellemeyer, H. L. Kyle and the Nimbus-7 Cloud Data Processing Team, 1989: Nimbus-7 global cloud climatology. Part II: First year results. *J. Climate,* **2**, 671–709.

_____, E. P. McClain, R. Carey, P. Pellegrino, G. Gutman, P. Davis, C. Long and S. Hart, 1991: Global distribution of cloud cover derived from NOAA/AVHRR operational satellite data. *Adv. Space Res.*, **11**, 51–54.

Takano, Y., and K. N. Liou, 1989: Solar radiative transfer in cirrus clouds. Part I: Single-scattering and optical properties of hexagonal ice crystals. *J. Atmos. Sci*., **46**, 3–19.

______ , and ______, 1995: Radiative transfer in cirrus clouds. Part III: Light scattering by irregular ice crystals. *J. Atmos. Sci*., **52**, 819–837.

Tsay, S. C., K. Stamnes and K. Jayaweera, 1989: Radiative energy balance in the cloudy and hazy Arctic. *J. Atmos. Sci.*, **46**, 1002–1018.

______ , ______ and ______ , 1990: Radiative transfer in planetary atmospheres: Development and verification of a unified model. *J. Quant. Spectrosc. Radiat. Transfer*, **43**, 133–148.

Twomey, S., and T. Cocks, 1982: Spectral reflectance of clouds in the near-infrared: Comparison of measurements and calculations. *J. Meteor. Soc. Japan*, **60**, 583–592.

_____. and _____, 1989: Remote sensing of cloud parameters from spectral reflectance in the near-infrared. *Beitr. Phys. Atmos.*, **62**, 172–179.

van de Hulst, H. C., 1974: The spherical albedo of a planet covered with a homogeneous cloud layer. *Astron. Astrophys.*, **35**, 209–214.

_____, 1980: *Multiple Light Scattering: Tables, Formulas, and Applications*, Vols. 1, Academic Press, New York, 76–82.

Vane, G., R. O. Green, T. G. Chrien, H. T. Enmark, E. G. Hansen, and W. M. Porter, 1993: The Airborne Visible/Infrared Imaging Spectrometer (AVIRIS). *Remote Sens. Environ.*, **44**, 127–143.

Wang, M., and M. D. King, 1997: Correction of Rayleigh scattering effects in cloud optical thickness retrievals. *J. Geophys. Res.*, **102**, 25915–25926.

Wetherald, R. T., and S. Manabe, 1988: Cloud feedback processes in a general circulation model. *J. Atmos. Sci.*, **45**, 1397–1415.

Wu, M. L. C., 1985: Quality of remote sensing measurements of cloud physical parameters in the Cooperative Convective Precipitation Experiment. *J. Geophys. Res.*, **90**, 10551–10562.

Yang, P., and K. N. Liou, 1995: Light scattering by hexagonal ice crystals: Comparison of finite difference time domain and geometric optics models. *J. Opt. Soc. Am. A*, **12**, 162–176.

_____. and _____, 1996a: Finite difference time domain method for light scattering by small ice crystals in three dimensional space. *J. Opt. Soc. Am. A*, **13**, 2072–2085.

_____. and _____, 1996b: A geometric optics/integral-equation method for light scattering by nonspherical ice crystals. *Appl. Opt.*, **35**, 6568–6584.

Appendix. *Acronyms*

AERI	Atmospheric Emitted Radiation Interferometer
AERONET	Aerosol Robotic Network
AirMISR	Airborne MISR
AM-1	First EOS morning polar-orbiting satellite
ARM	Atmospheric Radiation Measurement Program
ARMCAS	Arctic Radiation Measurements in Column Atmosphere-surface System (Beaufort Sea, Alaska, June 1995)
ASTEX	Atlantic Stratocumulus Transition Experiment (Azores, June 1992)
ASTER	Advanced Spaceborne Thermal Emission and Reflection radiometer
ATBD	Algorithm Theoretical Basis Document
AVHRR	Advanced Very High Resolution Radiometer
AVIRIS	Airborne Visible/Infrared Imaging Spectrometer
BRDF	Bidirectional Reflectance Distribution Function
CAR	Cloud Absorption Radiometer
CCN	Cloud Condensation Nuclei
CEPEX	Central Equatorial Pacific Experiment (Fiji, February-March 1993)
CERES	Clouds and the Earth’s Radiant Energy System
CLS	Cloud Lidar System
COARE	Coupled Ocean-Atmosphere Response Experiment
DAAC	Distributed Active Archive Center
DAO	Data Assimilation Office (NASA Goddard Space Flight Center)
ECS	EOSDIS Core System

EOS	Earth Observing System
EOSDIS	EOS Data and Information System
ER-2	Earth Resources high-altitude research aircraft (U2-R)
FIRE	First ISCCP Regional Experiment (California, June-July 1987, Beaufort Sea, Alaska, April-June, August 1998)
GCM	General Circulation Model
HIS	High-spectral resolution Interferometer Sounder
ISCCP	International Satellite Cloud Climatology Project
MAS	MODIS Airborne Simulator
MAST	Monterey Area Ship Tracks Experiment (Monterey and nearby Pacific Ocean, June 1994)
MCR	Multispectral Cloud Radiometer
MCST	MODIS Characterization Support Team
MISR	Multi-angle Imaging SpectroRadiometer
MODIS	Moderate Resolution Imaging Spectroradiometer
MOPITT	Measurement of Pollution in the Troposphere
NASA	National Aeronautics and Space Administration
NCEP	National Center for Environmental Prediction (NOAA)
NIR	Near-Infrared
NOAA	National Oceanic and Atmospheric Administration
NSA	North Slope of Alaska
PM-1	First EOS afternoon polar-orbiting satellite
RAMS	Radiation Measurement System (Scripps Institution of Oceanography)
SARB	Surface and Atmosphere Radiation Budget (CERES Working Group)

SCAR-A	Sulfate, Clouds and Radiation–Atlantic (Delmarva Peninsula and near-by Atlantic Ocean, July 1993)
SCAR-B	Smoke, Clouds and Radiation–Brazil (Brazil, August-September 1995)
SCAR-C	Smoke, Clouds and Radiation–California (Pacific Northwest, September 1994)
SCF	Science Computing Facility
SDST	MODIS Science Data Support Team
SGP	Southern Great Plains
SSFR	Spectral Solar Flux Radiometer (NASA Ames Research Center)
SUCCESS	Subsonic Aircraft Contrail and Cloud Effects Special Study (April-May 1996)
SWIR	Shortwave Infrared
TIROS	Television Infrared Observation Satellite
TLCF	Team Leader Computing Facility
TOGA	Tropical Ocean Global Atmosphere